

## PhD thesis in “Cotutelle”

University of Calabria - Italy

University Tunis El Manar - Tunisia

Science and Technologies of the Mesophases and the Molecular Materials  
STM<sup>3</sup> – International doctorate – XIX cycle

### PhD Thesis

### Order reconstruction in nematics

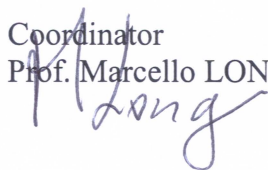
Supervisor

Prof. Riccardo BARBERI



Coordinator

Prof. Marcello LONGERI



Supervisor

Prof. Abdelhafidh GHARBI



Candidate

Habib AYEB



---

Academic Year 2005/2006



## PhD thesis in “Cotutelle”

University of Calabria - Italy

University Tunis El Manar - Tunisia

Science and Technologies of the Mesophases and the Molecular Materials  
STM<sup>3</sup> – International doctorate – XIX cycle (FIS/01)

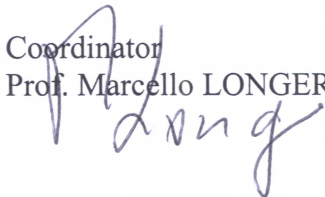
### PhD Thesis

### Order reconstruction in nematics

Supervisor  
Prof. Riccardo BARBERI



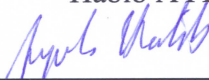
Coordinator  
Prof. Marcello LONGERI



Supervisor  
Prof. Abdelhafidh GHARBI



Candidate  
Habib AYEB



---

Academic Year 2005/2006



# Contents

Chapter 0 : <b>Introduction</b>	1
Chapter 1 : <b>General properties of nematic liquid crystal</b>	7
1.1. Nematic liquid crystal: An overview	10
1.1.1. Nematic Phase	11
1.1.2. Order and orientation	12
1.2. Physical properties of a nematic phase	14
1.2.1. Dielectric anisotropy	15
1.2.2. Birefringence	16
1.2.3. Viscosity	17
1.2.4. Elastic constants	18
1.2.5. Order electricity and flexo-electricity	19
1.3. Free energy of a nematic phase	20
1.4. Anchoring properties	23
1.5. Defects	25
Chapter 2 : <b>Electro-optical nematic devices</b>	29
2.1. Existing technologies	32
2.1.1. Monostable nematic display	32
2.1.2. Twist nematic (TN) mode	33
2.1.3. Guest-Host (G-H) mode	34
2.1.4. In-Plane Switching (IPS) mode	35
2.1.5. Bistable nematic displays	36
2.1.5.1. Bistable cholesteric display	37
2.1.5.2. Bulk Bistable Twisted Nematic (360°) display	38
2.1.5.3. Surface nematic bistability	39
2.1.5.4. Bistable Nematic Mode (BiNem)	40
2.1.5.5. Zenithal Bistable Display (ZBD)	41
2.2. A new technology: the nematic order reconstruction induced by electric field	43

<b>Chapter 3 : Numerical techniques</b>	<b>45</b>
3.1. <i>Q</i> -tensor versus vector representation	47
3.2. Computer simulations of physical systems	49
3.3. Modeling of the <i>Q</i> -tensor dynamic inside a LC cell	50
3.4. <i>Q</i> -tensor distribution update theory	52
3.5. Potential profile update theory	55
3.6. FEM implementation	56
3.7. Example 1D-solution	58
<b>Chapter 4 : Experimental techniques</b>	<b>65</b>
4.1. Cells construction	67
4.2. Surface characterization	69
4.3. Electro-optical setup	75
4.4. Liquid crystal material	79
4.5. Typical optical observations	80
<b>Chapter 5 : Results and discussion</b>	<b>83</b>
5.1. First investigations on the electric field induced order reconstruction	85
5.2. Nematic order reconstruction in symmetric cells	87
5.2.1. Typical observations	87
5.2.2. Order reconstruction dynamics	89
5.2.3. Bulk order reconstruction in symmetric cells	92
5.3. Nematic order reconstruction in asymmetric cell	99
5.3.1. Numerical investigations of asymmetric cell	99
5.3.2. Experiments with asymmetric cells	105
5.4. Experiments with doped nematics	109
5.4.1. Doping with MBBA	110
5.4.2. Doping with RM257	111
5.4.3. Doping with ferroelectric particles BaTiO <sub>3</sub>	112
<b>Chapter 6 : Conclusion</b>	<b>115</b>
<b>Bibliography</b>	<b>119</b>

# ACKNOWLEDGMENTS

It is perhaps not possible to express in words my gratitude to my research supervisor Prof. R. Barberi. I thank him for giving me the opportunity for this PhD, and for guiding me. His ideas, critical view, and a sharp eye for problems and solutions were indispensable for this work and have made me a better physicist. Every time I came to him with a problem, he either solved it or gave me new ideas that eventually lead to a solution. This has thought me that the cooperation and exchange of ideas are an integral part of scientific research.

I am eternally grateful to my co-supervisor, Prof. A. Gharbi, you always inspire me and show me the way how to proceed in research as well as in life matters, without your generous guidance I would not be able to achieve this opportunity. This has really meant a lot to me, I always felt that you stood behind me.

Many thanks, Ing. G. Lombardo, for your years of supervision, suggestions, guidance, teachings and your willingness to listen when I needed to talk about everything in the numerical calculations.

Thanks, Dr. F. Ciuchi, you always give me very helpful suggestions to do the experiments and for my thesis writing.

Thanks, Dr. M. De Santo, for AFM observations and your encouragement. My thanks also go out to C. Provenzano, G. Carbone, B. Zappone, T. Rugiero and A. Matranga for their help during these last three years. Thanks to all the people in the LiCryL research group and its coordinator Prof. R. Bartolino.

Many thanks to O. Pizzino and A. Pane for technical support in the clean room and for cells preparation.

Big thanks go to the coordinator Prof. Dr. M. Longeri for organising such a fantastic international Ph.D program and providing me a life time opportunity to participate in different scientific conferences.

I would also like to thank Dr. A. Glushchenko for providing the BaTiO<sub>3</sub> material, many thanks to Dr. G. Durand and Prof. E. Virga for their useful discussions and suggestions.

I wish to thank all the people in Tunisia who have helped me in several ways. Everyone has been a part of my experience here in Italy and the assistance I've received and friendships I've made will never be forgotten.

I thank the University of Calabria for giving me Scholarship for PhD.

Big thanks go to my brothers for their extra financial support for making things easier throughout my stay in Italy I also like to thank my sisters for their prayers and encouragements.

Finally, I owe all of my accomplishments to my parents. My father and mother, they sacrificed much to provide me with the quality of life from which I could choose what I want to be and to do. This thesis is dedicated to them both, with love and thanks for all they have done for me throughout my life.

# **CHAPTER 0**

**~Introduction~**





# Chapter 0

## Introduction

Since the discovery of electro-optical effects in liquid crystals in 1968, their main applications have been in the field of display technologies. The applications of liquid crystal displays now range from mobile telephones, digital cameras, portable DVD players, handheld games, PDAs, pictures viewers, flat computer screens, to, most lately, flat LCD TVs. The first practical device was the Twisted Nematic (TN) display. The TN cell was mostly used in the wrist-watch type of displays and can employ different types of nematic compounds, quite similar to 5CB, the nematic used in this work. In order to meet the requirements for more sophisticated displays, such as those used in cellular phones or laptop computers, more advanced display cells have been designed. The first important improvement was the Super-Twisted Nematic (STN) device. This is a direct refinement of the TN device, but with more advanced mesogens and cell geometry allowing a twist of  $270^\circ$  instead of  $90^\circ$  as for TN. This results in a sharper and faster transition between the bright and dark states. Further refinements have been achieved by improving the addressing of the display's individual pixel. This led to the development of the active matrix TFT displays, which are to nowadays the most used in the fabrication of screens for desktop and laptop computers and for flat LCD TVs. In the TFT active matrix technology each individual pixel has a thin film transistor (or diode) acting as a switch, which keeps the charge at the pixel electrodes almost constant. With the help of these TFTs, it is possible nowadays to manufacture displays having more than two million pixels (UXGA resolution: 1600 x 1280). Moreover, in the case colour of displays, each pixel is subdivided

into the three primary colors (RGB: red, green, and blue). That means, for example, that a UXGA resolution screen used in a large-area LCD monitor needs a total of about six million independently addressed pixels and the same number of TFTs, which makes this technology very delicate and quite expensive.

The current trend is towards the development of bistable displays. In fact, a bistable device, having two stable states in the absence of electric field, is capable of practically unlimited multiplexing, leading to high resolution and fast addressing on a passive matrix. This results in the elimination of the active matrix thin film transistor addressing technique. Furthermore, in bistable devices the external power is required only when the image is changed. The main advantages of such displays are their reduced power consumption, which is of crucial importance in portable devices, and their intrinsic memory. Since the early 1980s, nematic, cholesteric and smectic bistable liquid crystal technologies have been proposed. Indeed, many authors have proposed bulk switching mechanisms between bistable bulk textures, to create bistable nematic pixels. In spite of the recent improvements of the bulk switching devices, they remain relatively slow (driving pulses duration of several ms) and inefficient for any application. Fifteen years ago, surface switched bistable nematic displays were presented. The switching between these bistable textures was obtained by breaking the surface anchoring on the containing plates, giving fast write time in the microseconds range.

Recently, the electrically controlled nematic order reconstruction of the nematic bulk has been proposed as a new tool to achieve electrically controlled switching between two nematic textures with distinct topologies. This electro-optical effect is very fast, again in the microseconds range, and it implies the dynamical exchange of two eigenvalues of the nematic order tensor through intermediate biaxial states, likewise in the static case of crossing the core of a nematic defect.

The subject of this work concerns the deep characterization of the switching between two topologically distinct textures by high electric field and nematic order reconstruction.

The first chapter is an introduction to liquid crystals in general and to the nematic phase in particular, which will be of interest in this work. We detail the physics properties of the nematic liquid crystal mesophase.

The second chapter is dedicated to present the switching modes of liquid crystal devices. We start by presenting the different existing switching mechanisms in use in the liquid crystal device technologies and then we present the order reconstruction transition in nematic cells.

The third chapter concerns the description of a novel numerical model using the  $Q$ -tensor representation method. We then give an example of solution in the one-dimensional case. This model will be used in the following for a better understanding of the experimental results with solutions extended to the bi-dimensional case.

The fourth chapter describes the experimental techniques used for our investigations. We start by detailing the procedure of cells preparation and then we describe the technique of characterization of the different liquid crystal alignment layers used in this work. Finally, we present the electro-optical set-up used to investigate the nematic order reconstruction behaviour.

The fifth chapter is devoted to results and discussion. We start by a brief summary of the experimental and theoretical studies of the nematic order reconstruction. We then present our experimental results and we compare them to the theory by studying first symmetric cells and then asymmetric cells. Finally, we investigate the possibility to enhance the transient biaxial order in uniaxial nematics by suitable dopants.

The sixth chapter contains the conclusions of this work.



# **CHAPTER I**

**~~General properties of nematics ~~**

**Fundamentals**



# Chapter1

## General properties of nematics - Fundamentals

Liquid crystals (LC) are a phase of matter whose order is intermediate between that of an isotropic liquid and that of a crystal. For this reason they are more properly indicated as “mesophases”. Their molecules have anisotropic shapes and present non-uniform distributions of electric charges, usually resulting in a dipole. In this milky or cloudy fluids a certain long range order exists between the molecules. A first classification of this materials is based on the degree of order: the nematic phase, for example, is characterized by the orientational order of the constituent elongated molecules and the smectic phases, which are found at lower temperatures than the nematic, form well-defined layers that can slide over one another like soap. Of particular interest are phases of chiral molecules that, for instance, form the cholesteric texture, a nematic structure characterized by a spontaneous twist.

Liquid crystals are either calamitic (rod shaped) or discotic (disc like). Their phase transitions can be temperature driven (thermotropic mesogens) or density driven (lyotropic mesogens).



The typical calamitic and thermotropic liquid crystal molecule has two or more ring structures in the center with terminal chains on each end. Their typical dimensions are a length of the order of 20-30Å and a diameter of about 5Å [1]. The liquid crystal used in this work is a thermotropic nematic made up of individual rod-like molecules, and it is classified as a calamitic.

## 1.1. Nematic liquid crystal: An overview

To describe the main features of a nematic phase a first idealization is to consider the molecules on the average like long cylindrical rods or ellipsoids (elongated shapes). Figure 1.1 shows an artistic representation of the dependence of the phase order on temperature for a plausible thermotropic nematic material.

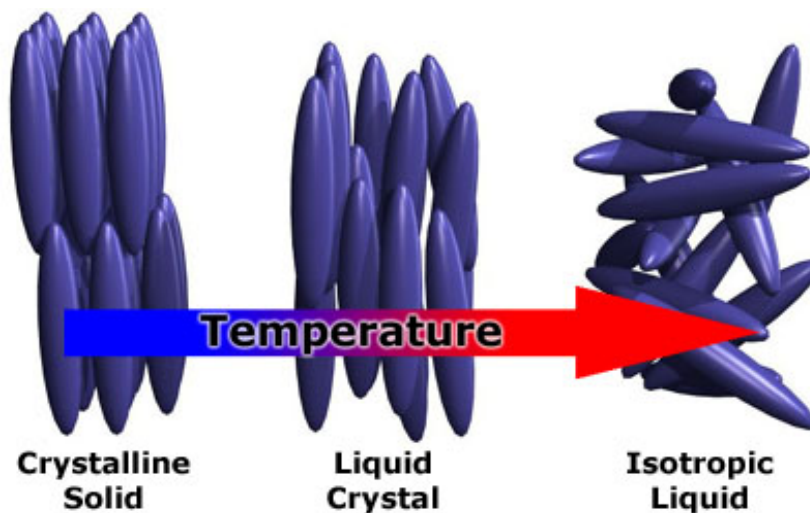


**Figure 1.1.** Schematic illustration of the solid, liquid crystal and isotropic liquid phases. The elliptical shapes represent the rod-like molecules.

### 1.1.1. Nematic phase

Among all LC phases, in this thesis we will be concentrated only on the nematic mesophase. Nematic comes from the Greek prefix “nemato” meaning threadlike and it is used here because the molecules in the liquid form defects that looks like long threads. The nematic phase is the simplest liquid crystalline phase and can be formed by calamitic mesogens. These phase is usually stable at room temperature and its temperature range is limited by a solid phase at lower temperature and an isotropic phase at higher temperature. The nematic phase has the lowest ordering of all the mesophases. The molecules making up the nematic phase are arranged in such a manner that there is no positional order of their centres of mass, like in the isotropic liquid, but there is a long range orientational order. Figure 1.2 shows a schematic representation of a small volume of a nematic liquid crystal.



**Figure 1.2.** Typical molecular alignment in a nematic material.

### 1.1.2. Order and orientation

The way in which the molecules order and orient themselves in various mesophases is critical for the properties of the liquid crystal itself. For a single molecule, we can define  $\mathbf{a}_i$  to be a unit vector along the long molecular axis. This individual rod direction is a microscopic property, and needs to be extended to macroscopic world of ensembles to have physical meaning for systems such as liquid crystal displays (LCDs) or our macroscopic experiment. The director  $\mathbf{n}$  is defined to be the average direction of  $\mathbf{a}_i$ , and it is imposed by the boundary conditions and possibly also by external fields. For example the confining surface can be treated on the way that ensures the molecules point along a certain axis at the interface called the easy direction. If the liquid crystal is distorted, the director can vary in space and it is necessary to define the director field  $\mathbf{n}(\mathbf{r})$ . In principle, the direction of the  $\mathbf{n}$  vector is arbitrary in space and represents the direction of the optical axis of the system. Since, the axis has no macroscopic polarity,  $+\mathbf{n}$  and  $-\mathbf{n}$  are equivalent; the sign of the director has no physical meaning. Thus if the molecules have an electric dipole there will be as many “up” molecules as “down” ones. The cylindrical symmetry and the tendency to align along the director may be expressed via an angular distribution function  $f(\theta, \varphi, \psi)$  with the following conditions

$$f(\theta, \varphi, \psi) = f(\theta) \text{ and } f(\theta) = f(\pi - \theta) = f(\cos(\theta))$$

The simplest way of defining a measure of alignment is the scalar parameters  $S$ ,

$$S = \frac{1}{2} \langle (3 \cos^2 \theta - 1) \rangle = \int f(\theta) \frac{(3 \cos^2 \theta - 1)}{2} d\Omega \quad (1.1)$$

where, the brackets denote a spatial averaging and  $\theta$  is the angle between  $\mathbf{n}$  and an arbitrary axis (usually chosen to be  $\mathbf{z}$ ). Equation (1.1) is the second term (the quadrupole moment) of an expansion in Legendre polynomials. The zero-order is

in fact a constant term and the first term (the dipole moment) vanishes identically:  $\langle \cos(\theta) \rangle = \int f(\theta) \cos(\theta) d\Omega = 0$ : they hence are not suitable to describe the nematic order. For isotropic liquids  $S = 0$ , for perfect orientational order (solid)  $S = 1$ . Liquid crystals typically have  $0.2 < S < 0.6$  [1] and  $S$  decreases as the temperature increases as figure 1.3 shows.

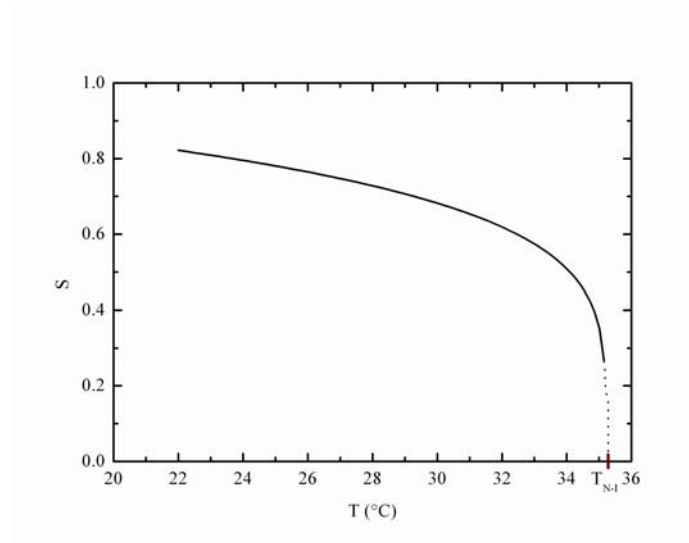


**Figure 1.3.** Dependence of the order parameter  $S$  on the temperature for a typical nematic, where  $T_{N-I}$  is the transition temperature from the nematic phase to isotropic liquid.

Describing a macroscopic order parameter we keep in mind the shape anisotropy of the constituent molecules, and we expect that several molecular response functions will be anisotropic. It is therefore appropriate to describe the degree of macroscopic order in terms of the tensor order parameter, also known as the  $Q$ -tensor. In general,  $Q$  is a rank-two, symmetric, traceless tensor and it has five independent scalar parameters. That is to say,  $Q = Q_{ij}$  ( $i, j = 1, 2, 3$ ) with  $Q_{ij} = Q_{ji}$  and  $\text{tr}(Q) = Q_{ii} = 0$  and it can be written as,

$$Q_{ij} = \frac{3}{2} N^{-1} \sum_k \left( a_i^{(k)} a_j^{(k)} - \frac{\delta_{ij}}{3} \right) \quad (1.2)$$

where the sum is over all the  $N$  molecules in a small but macroscopic volume located at  $r$ ,  $a^{(k)}$  is a unit vector along the axis of  $k$ -th molecule. The  $\delta_{ij}$  is the Kronecker's delta, which is 1 if  $i$  equals to  $j$ , and 0 otherwise. The tensor order contains information about the degree of order and the anisotropy of the liquid crystal at each point in space. The eigenvectors of  $Q$  give the directions of preferred orientation of the molecules while the eigenvalues  $\lambda_1$ ,  $\lambda_2$  and  $\lambda_3$  give the degree of order about these directions. The material is in an isotropic state if the three eigenvalues are equal. When two eigenvalues of  $Q$  coincide, the liquid crystal is in a uniaxial state, and finally, when all eigenvalues of  $Q$  are distinct, the liquid crystal is in a biaxial state.

## 1.2. Physical properties of a nematic phase

The rod-like shape of nematic liquid crystals means that their physical properties are anisotropic; that is, they exhibit different values when measured parallel or perpendicular to the director. This means that all dielectric, conductive, optical and mechanical properties depend upon the observation direction. The anisotropic nature of the physical properties of liquid crystals, due to their shape anisotropy, combined with the ability of magnetic and electric fields to influence the bulk spatial orientation render them of such importance to electro-optical devices. This section gives an overview of the dielectric, optical, elastic, viscous and surfaces properties of nematic liquid crystals.

### 1.2.1. Dielectric anisotropy

The interaction between a nematic and electric fields depends on the magnitude of the dielectric permittivity measured parallel  $\epsilon_{\parallel}$  and perpendicular  $\epsilon_{\perp}$  to the director. The dielectric anisotropy is defined as:

$$\epsilon_a = \Delta\epsilon = \epsilon_{\parallel} - \epsilon_{\perp} \quad (1.3)$$

The dielectric anisotropy can be both positive or negative and varies typically between +25 and -5 [1, 2]. The dielectric constants are dependent on the temperature and the frequency of the applied field. In electro-optical applications of liquid crystals, an electric field is applied to control the orientation of the liquid crystal molecules. The molecules of materials with  $\Delta\epsilon > 0$  try to align parallel to the field while materials with negative dielectric anisotropy align perpendicularly. Although liquid crystals with positive dielectric anisotropy are the most commonly used, both types can be found in applications depending on the switching principle. Because of the anisotropic nature of liquid crystals, the dielectric anisotropy is a tensor of range 2 and can be written as

$$\epsilon_{ij} = \epsilon_{\perp} \delta_{ij} + \Delta\epsilon n_i n_j \quad (i,j = x, y, z) \quad (1.4)$$

The components  $\epsilon_{ij} = \epsilon_{ji}$ ; i.e. the tensor is symmetric.

In the local frame of reference (with the  $\mathbf{z}$  axis along the director) has the form:

$$\epsilon'_a = \begin{pmatrix} \epsilon_{\perp} & 0 & 0 \\ 0 & \epsilon_{\perp} & 0 \\ 0 & 0 & \epsilon_{\parallel} \end{pmatrix} \quad (1.5)$$

### 1.2.2. Birefringence

Birefringence, or double refraction, is the decomposition of a ray of light into two rays (the ordinary ray and the extraordinary ray) when it passes through certain types of materials, such as liquid crystals, depending on the polarization of light. This effect can occur only if the structure of the material is anisotropic so that light behaves differently depending on which direction the light is propagating. Liquid Crystals are birefringent due to their anisotropic nature. Light polarized parallel to the director has different index of refraction (that is to say it travels at a different velocity) than light polarized perpendicular to the director. To be a little more quantitative, the index of refraction of a material is defined as the ratio of the speed of light in a vacuum to that in the material. For a nematic we have  $n_e = \frac{c}{v_e}$  and  $n_o = \frac{c}{v_o}$ , where  $c$  is the light velocity in the vacuum,  $v_{e,o}$  are respectively the velocity of light parallel and perpendicular to the director.  $n_o$  is the refractive index of the ordinary ray which is always perpendicular to the optic axis, so  $n_o$  is constant and independent of propagation direction, whereas  $n_e$  is the refractive index of the extraordinary ray and varies with the ray propagation angle  $\theta$  with respect to the optic axis according to

$$\frac{1}{n_{eff}(\theta)} = \frac{\cos^2(\theta)}{n_o^2} + \frac{\sin^2(\theta)}{n_e^2} \quad (1.6)$$

This relationship is illustrated by the refractive index ellipsoid as shown in figure 1.6. The birefringence magnitude then depends on the propagation direction and is defined by

$$\Delta n = n_e - n_o \quad (1.7)$$

If  $\Delta n > 0$ , the LC is said to be positive birefringent, whereas if  $\Delta n < 0$ , it is said to be negative birefringent. Most LCs with rod-like molecules exhibit a positive

birefringence ranging from 0.04 to 0.45 [2]. The optical birefringence plays an essential role in changing the polarization state of light in liquid crystal displays.

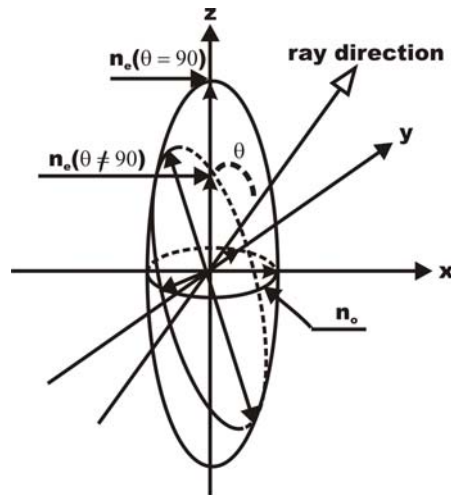


**Figure 1.4.** The refractive index ellipsoid of an uniaxial liquid crystal phase with the optic axis parallel to the z axis.

### 1.2.3. Viscosity

The viscosity of liquid crystalline state is also an anisotropic property, depending on the direction of flow of an individual molecule with respect to the director at any point within the medium. In the nematic phase there are three flow viscosities,  $\eta_a$ ,  $\eta_b$  and  $\eta_c$  also called Miesowisz viscosities.  $\eta_a$  is perpendicular to the direction of flow and parallel to the velocity gradient,  $\eta_b$  is parallel to the direction of flow but perpendicular to the velocity gradient and  $\eta_c$  is perpendicular to both flow direction and the velocity gradient. The bulk viscosity of a nematic phase is an average of these three viscosity coefficients. If the director is not held in its place, it will be affected by a hydrodynamic torque; it is then necessary to introduce the rotational viscosity  $\gamma_1$ . The rotational viscosity  $\gamma_1$  depends on the detailed



molecular constituents, structure, intermolecular association and temperature. As the temperature increases the viscosity decreases rapidly. Rotational viscosity is a very important parameter for LC devices. The time for director reorientation in presence of an electric field is given by  $\tau_{on} \propto \frac{\gamma_1 d^2}{\epsilon_0 \Delta\epsilon V^2}$  and  $\tau_{off}$  is the time necessary to restore the equilibrium configuration after the electric field is switched off.  $\tau_{off} \propto \frac{\gamma_1 d^2}{K}$  is usually longer than  $\tau_{on}$  since the electric torque is stronger than the elastic torque. For most nematic LCs used in displays, the magnitude of the rotational viscosity is in the range of 0.02 to 0.5 Pa.s [2].

#### 1.2.4. Elastic constants

Under mechanical stress, liquid crystals deform and try to restore the equilibrium configuration. The restoring torques are determined by the three elastic constants,  $K_{11}$ ,  $K_{22}$  and  $K_{33}$  that are associated with splay, twist and bend deformations respectively as figure 1.5 shows. The elastic constants co-determine the spatial and temporal response of the director to applied external electric field.

In calamitic liquid crystals one usually finds the following relation  $K_{33} > K_{11} > K_{22}$ . For most LC compounds, the elastic constants are in the range of 3-25 pN [2].

The ratio of the elastic constants varies from 0.7 to 1.8 for  $\frac{K_{33}}{K_{11}}$ , and from 1.3 to

3.2 for  $\frac{K_{33}}{K_{22}}$  [2].

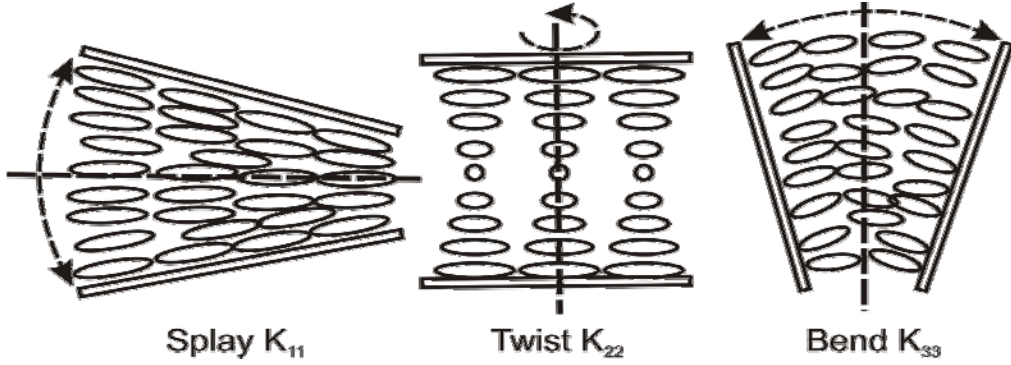


**Figure 1.5.** Schematic representation of the Frank elastic constants  $K_{11}$ ,  $K_{22}$  and  $K_{33}$  for Splay, Twist and Bend deformation respectively of a nematic phase.

### 1.2.5. Order electricity and flexo electricity

When the order parameter of a nematic liquid crystal close to a surface or an interface, differs from the order parameter in the volume, a surface polarization called ordo-electric polarization arises and is given by [3, 4]:

$$P_o = r_1 (\vec{n} \cdot \vec{\nabla} S) \vec{n} + r_2 \vec{\nabla} S \quad (1.8)$$

Where,  $r_1$  and  $r_2$  are the order electric coefficients of the interface.

In the case of a distorted nematic liquid cell (by action of an external electric field) a flexo-electric coupling arises between the electric field and the flexo-electric polarization which is given by [5]

$$P_f = e_{11} \vec{n} \cdot (\vec{\nabla} \cdot \vec{n}) - e_{33} \vec{n} \times (\vec{n} \times \vec{n}) \quad (1.9)$$

Where  $e_{11}$  and  $e_{33}$  are the flexo-electric splay and bend coefficients.

### 1.3. Free energy of a nematic phase

Two main forces determine the behaviour of a liquid crystal: elastic forces within the material which try to minimise energy by aligning the easy direction as requested by the geometry and electric forces that align the molecules along or perpendicular to the field. Adding the electric and the elastic deformation free energies together, the total free energy density is obtained:  $f_{\text{bulk}} = f_d + f_e$ . The first term describes the elastic energy density of the bulk under distortion of the director  $\mathbf{n}$  and following Oseen-Frank's theory can be written as [6]:

$$f_d = \frac{K_{11}}{2} (\vec{\nabla} \cdot \vec{n})^2 + \frac{K_{22}}{2} (\vec{n} \cdot (\vec{\nabla} \times \vec{n}))^2 + \frac{K_{33}}{2} (\vec{n} \times (\vec{\nabla} \times \vec{n}))^2 \quad (1.10)$$

Where,  $K_{11}$ ,  $K_{22}$  and  $K_{33}$  are the splay, twist and bend elastic constants respectively.

In principle, there are other contributions that should be added to the elastic free energy, namely the splay-bend and the saddle-splay cross terms [7, 8]:

$$f_{13} = \frac{K_{13}}{2} \vec{\nabla} \cdot (\vec{n} \cdot (\vec{\nabla} \cdot \vec{n})) \quad (1.11)$$

$$f_{24} = \frac{-K_{24}}{2} \vec{\nabla} \cdot (\vec{n} \times (\vec{\nabla} \times \vec{n}) + \vec{n} (\vec{\nabla} \times \vec{n})) \quad (1.12)$$

Where,  $K_{13}$  and  $K_{24}$  are the surface-like, splay-bend and saddle-splay elastic constants. In fact, the elastic term with the  $K_{13}$  is equal to zero [9, 10]. The term  $f_{24}$  must be considered when liquid crystals are confined in curved geometries or in a hybrid aligned nematic cells.

In the one elastic constant approximation ( $K_{11} = K_{22} = K_{33} = K$ ) the  $f_d$  can be simplified and given by:

$$f_d = \frac{K}{2} \left( (\vec{\nabla} \cdot \vec{n})^2 + (\vec{\nabla} \times \vec{n})^2 \right) \quad (1.13)$$

The second term of the free energy density represents the contribution of the electric energy density. Without taking into account the flexo-electric contribution, it is given by

$$f_e = -\frac{\vec{E} \cdot \vec{D}}{2} \quad (1.14)$$

The minus sign on the equation (1.14) comes from the fact that there is a constant electric potential  $U$  applied on the cell.

Integrating over the volume of the liquid crystal, we obtain the total bulk free energy

$$F_{bulk} = \int (f_d + f_e) dv \quad (1.15)$$

In the one constant approximation, using the one-dimensional co-ordinate, and if we suppose that the director remains always in the plane  $xz$ , because only zenithal torques is applied to it, the director is then  $\mathbf{n}(z) = (\sin\theta, 0, \cos\theta)$ , where  $\theta = \theta(z)$  is the zenithal angle between the director and the  $z$  axis. Equation 1.15 is then given by

$$F_{bulk} = \int \frac{K}{2} \left[ \left( \frac{d\theta}{dz} \right)^2 + \frac{\sin^2 \theta}{\zeta^2} dz \right] \quad (1.16)$$

Where  $\zeta = \sqrt{\frac{K}{\epsilon_0 \epsilon_a E^2}}$  is the electric coherence length, describing the response of the liquid crystal to an external electric field.

Dickman derived the  $Q$ -tensor form of the frank-Oseen strain free energy density [11-13]:

$$f_d = \sum_{i,j,k=1,2,3} \left[ \frac{L_1}{2} \left( \frac{\partial Q_{ij}}{\partial x_k} \right)^2 + \frac{L_2}{2} \frac{\partial Q_{ij}}{\partial x_j} \frac{\partial Q_{ik}}{\partial x_k} + \frac{L_3}{2} \frac{\partial Q_{ik}}{\partial x_j} \frac{\partial Q_{ij}}{\partial x_k} \right] + \sum_{i,j,k,l=1,2,3} \left[ \frac{L_4}{2} e_{lik} Q_{lj} \frac{\partial Q_{ij}}{\partial x_k} + \frac{L_6}{2} Q_{lk} \frac{\partial Q_{ij}}{\partial x_l} \frac{\partial Q_{ij}}{\partial x_k} \right] \quad (1.17)$$

The coordinates  $(x_1, x_2, x_3) = (x, y, z)$  are the usual Cartesian coordinate system and  $Q_{ij}$  is the  $ij^{\text{th}}$  element of  $Q$ . The elastic parameters  $L_i$  are related to the Frank elastic constants  $K_{ij}$  and to the scalar order parameter. The Levi-Civita symbol  $e_{lik}$  is 1 when subscripts are in the order of xyz, yzx, or xzy, and is -1 if the subscript order is xzy, yxz, or zyx, 0 otherwise.

The  $Q$ -tensor form of the electric energy density is derived directly from equation (1.18) where the flexo-electric effect is considered and it can be written as,

$$f_e = -\frac{\vec{E} \cdot \epsilon_0 (\epsilon \vec{E})}{2} - \vec{E} \cdot \vec{P}_f \quad (1.19)$$

The dielectric tensor is approximated to be  $\epsilon = \Delta \epsilon^* Q + \bar{\epsilon} I$  where  $\Delta \epsilon^* = \Delta \epsilon / S$  with  $\Delta \epsilon = \epsilon_{\perp} - \epsilon_{\parallel}$  and  $\bar{\epsilon} = (2\epsilon_{\perp} + \epsilon_{\parallel})/3$ .  $P_f$  is the spontaneous polarisation and it is assumed to drive only from a flexo-electric type of polarisation. In other words, the flexo-electric effect describes the spontaneous polarization caused by a deformation of the nematic molecular arrangement. This distortion of the director may be due to a shape asymmetry in molecules that have permanent dipole moments. The spontaneous polarization  $P_f$  can be written in terms of  $Q$ -tensor as [14],

$$P_f = \bar{e} \nabla \cdot Q \quad (1.20)$$

Where  $S \bar{e} = (e_{11} + e_{33})/2$  in which  $e_{11}$  and  $e_{33}$  are the splay and bend flexo-electric coefficients respectively, with the  $i^{\text{th}}$  component of  $\nabla Q$  is understood to be  $\sum_{j=1,2,3} \partial Q_{ij} / \partial x_j$ .

Using the relationship  $E = -\text{grad}(V)$  and equation (1.19), the electric free energy density can be expressed in terms of the  $Q$ -tensor as

$$f_e = -\frac{\epsilon_0}{2} \left( \bar{\epsilon} U_j^2 + \Delta \epsilon U_j U_{,k} \frac{Q_{jk}}{S} \right) + U_j \bar{e} \nabla Q \quad (1.21)$$

where  $U_j = \frac{\partial U}{\partial x_j} \quad j = 1 \dots 3$

## 1.4. Anchoring properties

The anchoring phenomenon is the tendency of a liquid crystal to orient in a particular direction when in contact with confining surfaces. Close to the interface the nematic molecules take a fixed mean orientation which is called the anchoring direction (easy axis) of the liquid crystal at the interface, defined by the angles  $(\theta_e, \varphi_e)$ .

- Planar alignment: the director aligns parallel to the cell surface.
- Homeotropic alignment: the molecular director is perpendicular to the cell surface.
- Tilted anchoring: the director is tilted at any angle different from  $0^\circ$  and  $90^\circ$  with respect to the surface.

The simplest form of the surfaces anchoring density has been proposed by Rapini and Papoular [15]:

$$f_s = \frac{W_\theta}{2} (\sin \theta)^2 + \frac{W_\phi}{2} (\sin \varphi)^2 \quad (1.22)$$

Where the parameter,  $W_\theta$  and  $W_\phi$  are the zenithal and azimuthal anchoring strength coefficients respectively. Numerous experimental methods have been used to measure the surface anchoring coefficients  $W_\theta$  and  $W_\phi$ , by measuring surface director deviations in an external field. All measurements of anchoring strength give values of  $W_\theta$  and  $W_\phi$  ranging between  $10^{-7}$  and  $10^{-3} J/m^2$  [16].

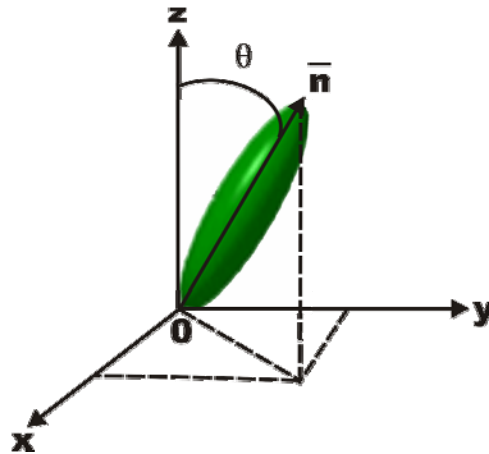


**Figure 1.6.** Definition of the zenithal anchoring angle.

## 1.5. Defects

Topological defects appear in physics as a consequence of broken continuous symmetry. They exist almost in every branch of physics and mainly in crystalline physics and liquid crystal physics. Liquid crystals are ideal candidate for studying topological defects. First explanations of defects in nematic liquid crystals were given by Friedel who suggested that these defects are lines in which the director changes its direction discontinuously. In analogy with dislocations in crystals, Frank proposed to call them disclinations [17]. Because of the birefringence of nematic, these disclinations can be recognised optically. To classify topological defects the homotopy theory can be employed to study the order parameter space [18]. In nematics there are two kinds of stable topological defects in three dimensions: point defects and line defects. Moving around the disclination the director undergoes a rotation of  $2\pi m$ , where  $m$  can be integer or half-integer and it is called defect strength. Depending on the direction of rotation of the director,  $m$  is positive when the director rotation is clockwise, otherwise  $m$  is negative. Examples of disclinations for several  $m$  are given in figure 1.9. In a nematic with a vector order parameter is not possible to describe a topological defect since it lacks the inversion symmetry of the nematic phase with respect to the director. Schopohl and Sluckin [19] proposed a static model of the core of a nematic defect using the Landau-de Gennes free energy which employs the second-rank tensor  $Q$  as an order parameter. The tensor  $Q$  also describes the biaxial liquid crystalline order. Investigations showed that the core of a disclination should indeed be biaxial, with a core radius of the order of the biaxial correlation length  $\zeta_b$  (figure 1.10). Outside of the defect core, the nematic order is essentially uniaxial. Therefore the core energy is determined by the energy difference between the biaxial and uniaxial states rather than the energy difference between the isotropic and nematic state.



Defects play important roles away from phase transition points, e.g., in the equilibration process following a quench from a disordered to an ordered phase (“coarsening dynamics”). Defects also arise in other physical situations, e.g. in the case of liquid crystals, the confinement of the material naturally leads to the formation of defects given the interplay between surface anchoring and bulk elastic energy. The dynamics of defects of liquid crystals is also of technological importance, e.g., in displays based on multi-domain cells. In general, defects occur to allow for the transition between topologically inequivalent director configurations as in the case of the well known  $\pi$ -cell. Usually, the starting director configuration of the  $\pi$ -cell is the splay state, and by applying a voltage the director configuration goes to the bend state. This transition between the topologically inequivalent splay and bend states is necessarily associated with defects. Moreover, as it will be shown in the following, it exists a strong analogy between the order variation inside a static nematic defect and the dynamical evolution of the nematic order for a bulk splay-bend transition.

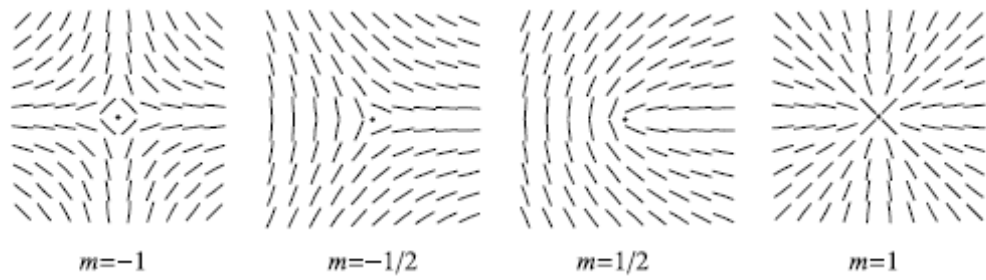


**Figure 1.7.** Director fields surrounding topological defects of different strength  $m$ .

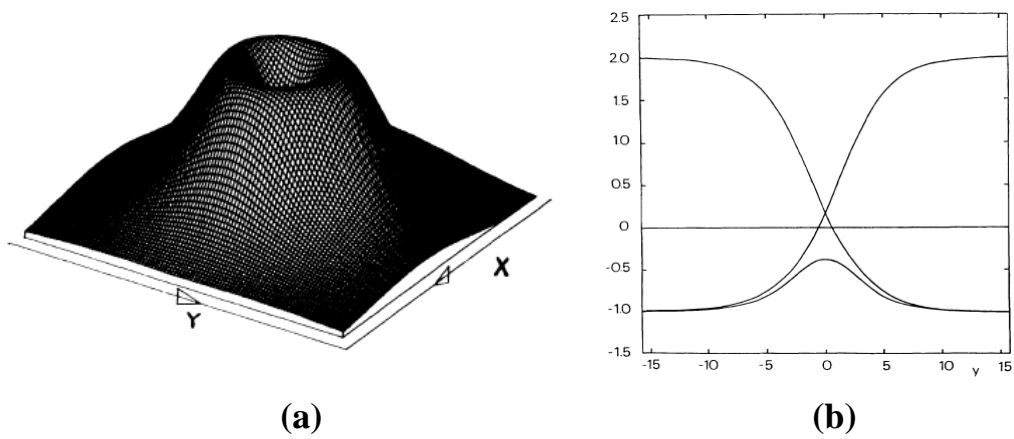


**Figure 1.8.** (a) Energy surface of a nematic defect for  $m = -1/2$ , (b) values assumed in space by the  $Q$  eigenvalues for the same defect [19].  $y = 0$  represents the centre of the defect.



# **CHAPTER II**

**~Electro-optical nematic devices~**



## Chapter 2

### Electro-optical nematic devices

Since Heilmeyer et al. introduced the first liquid crystal display prototype in the late 1960's, active developments for new display modes have been underway. This continuous activity made use of many varieties of nematic materials, molecular surface alignment states and pixel structures. Up to now, several possibilities for the application of liquid crystal in displays have been presented. Dynamic scattering mode, Ferroelectrics, Guest-Host, Polymer Dispersed Liquid Crystals (PDLC), etc... is only a short list of technologies, which finally turned out to be not successful for actual commercial display applications. Currently, almost all liquid crystal displays use nematics with some kind of super twisted texture and active TFT addressing.

In this chapter, we give an overview about the more useful liquid crystal systems, both monostable or that exhibit two stable states under zero electric field, but electrically switchable. Intrinsic bistability is in fact desirable for novel potential display applications. These bistable systems can be classified into two groups: first, the bulk bistable devices having two distinct textures without changing the boundary conditions; second, surface controlled bistability where the surface anchoring is modified.

## 2.1. Existing technologies

### 2.1.1. Monostable nematic display

The basic component of an LCD is a thin layer of liquid crystal sandwiched between a pair of conductive glass plates and excited by a suitable external electric field which changes the texture (figures 2.1 and 2.2). In absence of the external electric field, the nematic layer is in an equilibrium configuration, which corresponds to a minimum of its elastic free energy. The application of an electric field between the electrodes changes the texture of the nematic, which goes into an excited configuration and then relaxes back to its starting equilibrium stable state when the electric field is shut off. These systems are bulk monostable because they always go back to the unique equilibrium stable structure with no field applied (figure 2.2). This is the well-known *Freedericks* transition [1]. For most displays, a minimum field (threshold) is necessary to switch molecules. The critical electric field  $E_{th}$  that causes the transition of the molecular alignment can be expressed by  $E_{th} = (\pi/d) \sqrt{K_{ii} / \epsilon_0 \Delta\epsilon}$  where,  $K_{ii}$  is  $K_{11}$  for splay,  $K_{22}$  for twist and  $K_{33}$  for bend deformation. For other display structures that employ different deformations at the same time, the above expression is more complicated.

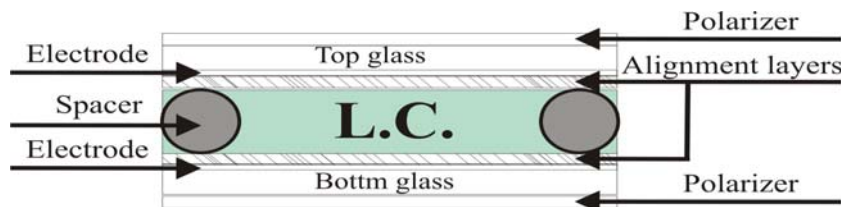


**Figure 2.1.** The structure of a typical nematic LCD.

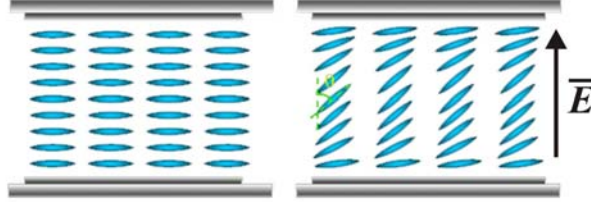


**Figure 2.2.** Planar nematic cell before and after the application of an electric field respectively.

### 2.1.2. Twist Nematic (TN) mode

The twisted-nematic (TN) mode is the most mature LCD mode. It was first introduced by Schadt and Helfrich, and also by Fergason in 1971[20, 21]. A typical TN-LCD consists of a nematic liquid crystal enclosed in a cell with rubbed polyimide alignment layers. The direction of the planar alignment at the upper substrate is orthogonal to that at the lower substrate. Then the director will twist from one electrode to the other over  $90^\circ$  in the off state (figure 2.3). The two polarizers are attached in a way that their polarization is parallel to the rubbing direction of the closer glass substrate. Because of the wave-guide regime, the polarization plane of the light will rotate over  $90^\circ$ , at the exit the light will pass through the analyzer, and the cell will be bright. When an electric field is applied perpendicular to the substrates, the molecules in the cell, due to their positive dielectric anisotropy will try to orient along the field. The LC layer no longer rotates the light polarization, so at the second polarizer, the light is blocked, and this is the black state. The critical electric field  $E_{th}$  that causes the orientation of liquid crystal molecules along the field is given by [2]:

$$E_{th} = (\pi/d) \sqrt{K_{11} / \epsilon_0 \Delta\epsilon (1 + (K_{33} - 2K_{22}) / 4K_{11})}$$



The first problem with the TN mode is that the black state cannot be achieved perfectly because the molecules at the alignment layers are still oriented homogeneously as a consequence of the strong anchoring on the surface. Another disadvantage is the limited viewing angle.

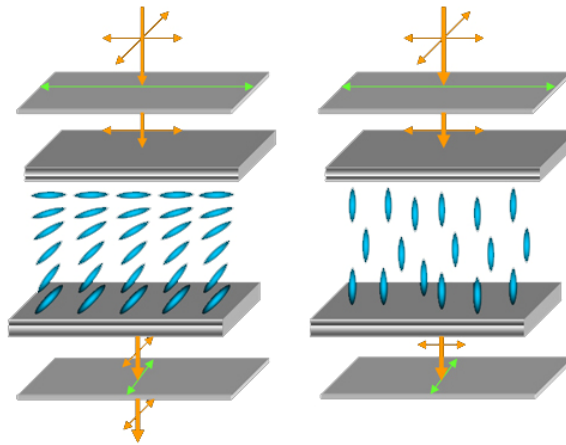


**Figure 2.3.** Twist Nematic Display mode.

### 2.1.3. Guest-Host (G-H) mode

In a Guest-Host system, the mixture is prepared by mixing liquid crystal (Host) and dichroic dyes (Guest) [22, 23]. The dye is chosen so that its maximum absorption axis aligns parallel to the director and so that the viscoelastic and dielectric properties of a nematic host are virtually unchanged. The dichroic dyes absorb the light when its E-field is along the long axis of the dye. When the liquid crystal molecules change their orientation, the dye will also re-orient along with LC molecules and also its absorption axis changes direction, modulating hence the light transmission. Several device configurations using Guest Host mode have been proposed. In this paragraph, we review White-Taylor GH display (figure 2.10) [24]. In the off state, the dye is in the cholesteric LC, the dye is oriented in

all directions due to rotating director. When the light passes through, it is strongly absorbed and the display appears coloured. In the on state, minimum absorption is present; hence, a white image is obtained. An interesting variation of this technology makes use of luminescent dichroic dyes and it does not need polarizers.

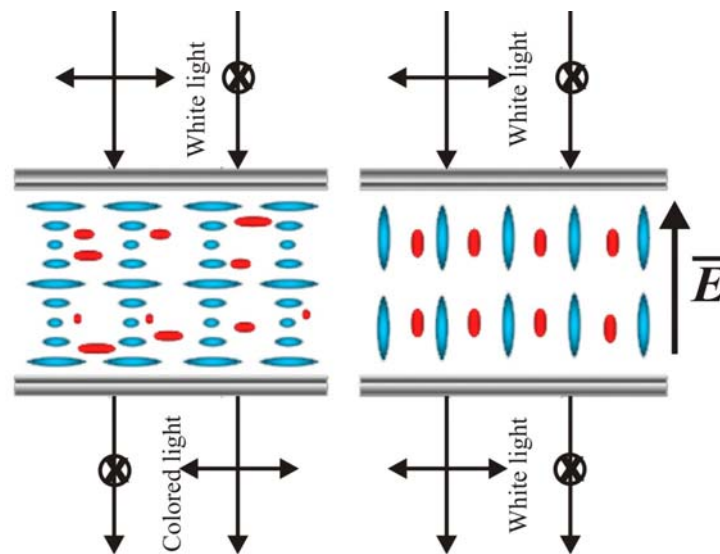


**Figure 2.4.** A White-Taylor GH-display.

#### 2.1.4. In-Plane Switching (IPS) mode

In the IPS display the reorientation upon switching takes place in a plane parallel to the substrates [25, 26]. This requires both electrodes to be constructed on the same side of one substrate. As shown in figure 2.11, the alignment layers on both substrates are rubbed at  $45^\circ$  with respect to the electrodes, the linearly polarized light enters the cell with polarization parallel to the director. The top polarizer is perpendicular to the bottom polarizer which is along the rubbing direction. Then the cell is dark in the off state. When voltage is applied, the electrodes

configuration creates an in-plane electric field in the bulk of the cell, and the molecules try to orient along the field, remaining in the plane of the electrodes. Under electric field twist structure appears and maximum transmission is reached when the molecules rotate  $45^\circ$  respect to the original state. This mode is very interesting for its very interesting optical properties and large view angle.

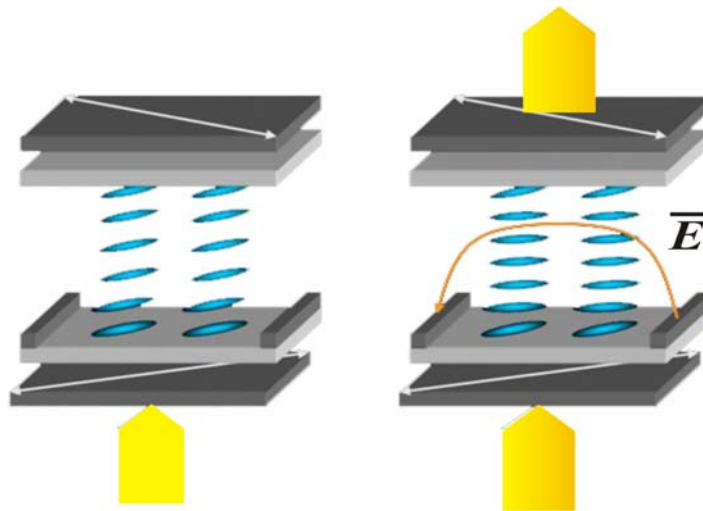


**Figure 2.5.** The operating principle of In-Plane-Switching mode.

### 2.1.5. Bistable nematic displays

The bistability is an interesting phenomenon for application in display technologies. In principle, bistability enables infinitely long memory time, infinite multiplexability and low power consumption. The basic idea to realize bistable configuration, is to connect through a field effect two topologically distinct textures that are in principle separated by an energy barrier (figure 2.3). Up nowadays, several bistable display technologies have been proposed, using nematic, cholesteric or smectic liquid crystal. Surface stabilized ferroelectric liquid crystals are fast and show good bistability but their drawback is the high

sensitivity to mechanical and thermal shocks. In this section, we present the most common bistable modes potentially useful for display technologies.

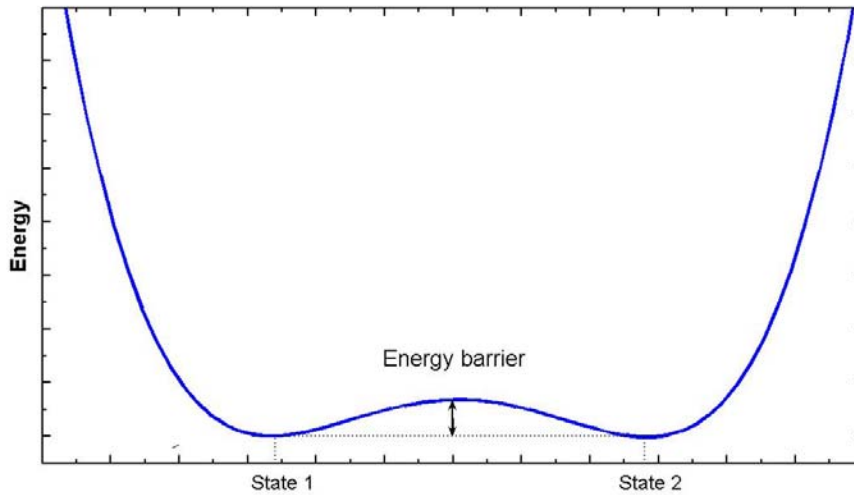


**Figure 2.6.** Degenerate minima energy states 1 and 2 of a true bistable system.

### 2.1.5.1. Bistable cholesteric display

The cholesteric display was proposed more than 30 years ago [27, 28] and it is based on order-disorder texture switching (figure 2.4). The cholesteric material consists of either chiral nematic molecules or a nematic liquid crystal with addition of chiral agents. This leads to a formation of a spontaneous helical twisting. The two stable textures are the planar and focal conic textures (figure 2.4). The planar texture reflects strongly one of the circular polarizations (it depends on the helicity of the cholesteric structure). The focal conic transmits the light, which is absorbed by the back plate, and the resulting state is dark. When a voltage is applied to the planar texture, a focal conic domain configuration is

obtained through an intermediate homeotropic state. Both the planar and focal conic domains are stable states, no field is required to maintain it, therefore bistability can be achieved. The form and amplitude of the driving pulse control dynamically the selection of the final state. This device is based on a simple idea, but the focal conic state is very difficult to be erased and hence its real performances are poor.

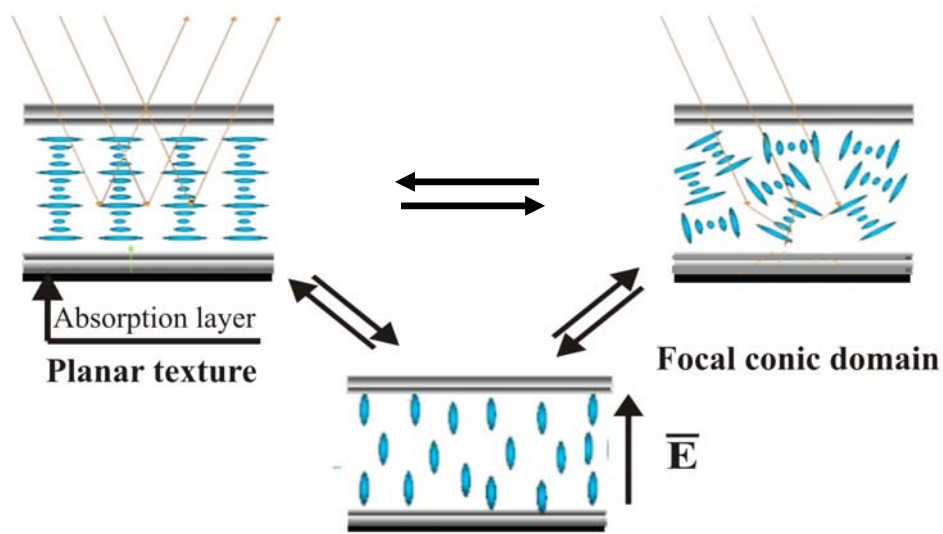


**Figure 2.7.** Textures realized in the bistable cholesteric display.

### 2.1.5.2. Bulk Bistable Twisted Nematic ( $360^\circ$ BTN) display

This device was proposed by Berreman et al. [29], and was based on two different twist states,  $0$  and  $360^\circ$ . The device uses strong monostable anchoring with high anti-parallel pre-tilt angles (figure 2.5). The energies of the two textures are equalized by adding a chiral agent to fix the pitch ratio ( $d/p$ ) about  $0.5$ . These two states are topologically equivalent and one can switch between them through an intermediate homeotropic state by applying a suitable electric field. In absence of

electric field the topologically different  $180^\circ$ -twisted state is usually energetically preferred. In fact, the device is metastable and when the electric field is switched off the  $360^\circ$  state relaxes to the  $180^\circ$  texture by defects propagation. There are no commercial applications of this cell due to the delicate addressing scheme it requires and to the quite long switching times.

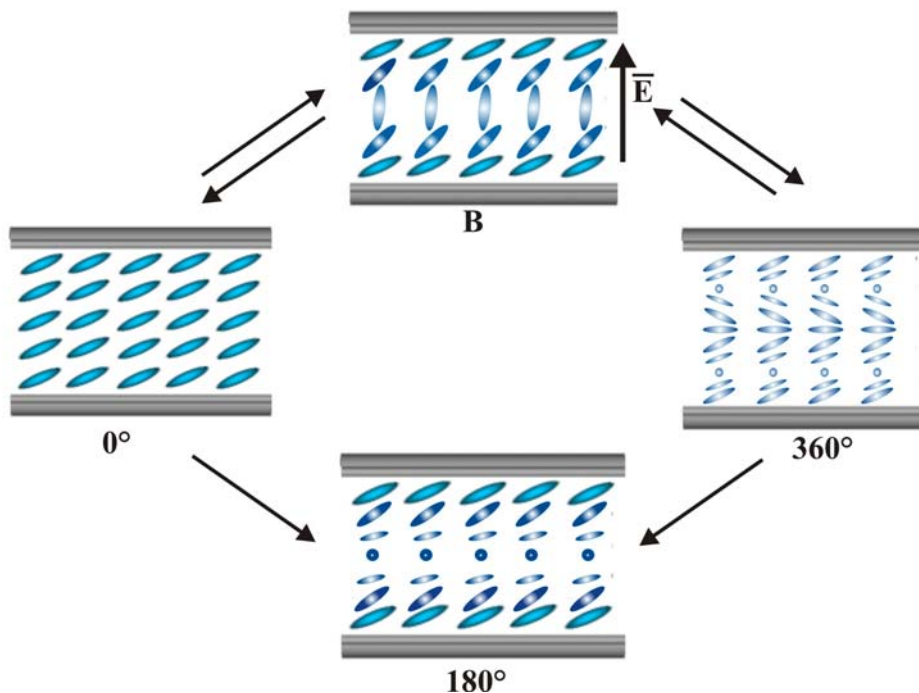


**Figure 2.8.** Textures and transitions in the Berreman's bistable twisted nematic.

### 2.1.5.3. Surface nematic bistability

Fifteen years ago, Barberi et al. [30, 31] proposed surface switched bistable nematic displays, based on bistable surface anchoring and anchoring breaking. They used two bistable textures with different azimuths or different tilt angles

(figure 2.6). The switching between these bistable textures is obtained by breaking the surface anchoring and the flexo-electric coupling enables to select the final state. The switching by breaking surface anchoring is very fast and can be controlled by pulses of a few  $\mu\text{s}$ , but in practice it is very difficult to realize the required bistable anchoring.

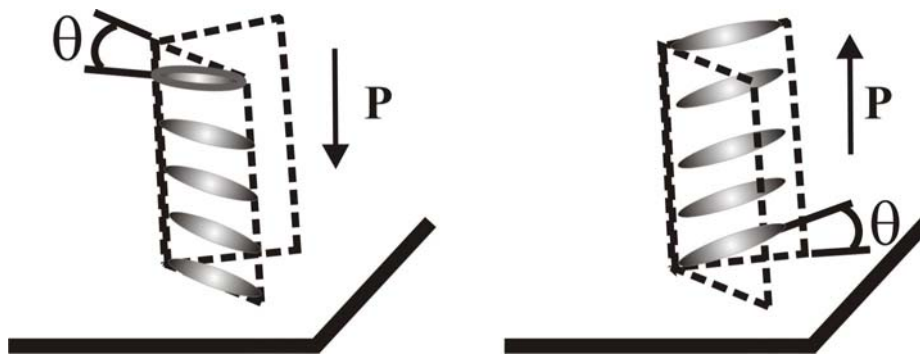


**Figure 2.9.** Flexoelectrically controlled nematic device using bistable surface.

#### 2.1.5.4. Bistable Nematic Mode (BiNem)

The BiNem mode was introduced by Durand et al. ten years ago and it is now under development by Nemoptic. It uses two different anchoring conditions on two substrates to achieve the bistability, usually one substrate is a weak planar anchoring and the other one has a strong tilted anchoring [32, 33]. The switching mechanism is based on the so called "*surface anchoring breaking*". The two-bistable textures are respectively at  $0^\circ$  (U) and  $180^\circ$  (T) (figure 2.7). The two states can be interchanged by applying different electric pulses. These two bistable textures are topologically distinct and cannot transform to one another by continues bulk deformation. When a strong electric field is applied, the bulk director is oriented along the field, except in a thin layer of thickness

$\zeta = \sqrt{K/(\epsilon_0 \Delta\epsilon E^2)}$  close to the surface. Above some critical field  $E_c$ , defined by  $\zeta = L_z$  where  $L_z$  is the zenithal extrapolation length, the anchoring angle is equal to  $90^\circ$ . After the surface relaxation, the surface director can be  $n_s$ , or  $-n_s$  giving two different bulk textures. The final state selection is obtained by the pulse waveform. If the field is switched off slowly, elastic coupling is favoured and the U state is selected. On the other hand, if the electric field is switched off instantaneously dynamic coupling is favoured and the sample relaxes toward the T state. The main advantages of this device are the simple monostable alignment layers and its long-term bistability. The main drawback is the difficulty to achieve uniform weak planar anchoring conditions.

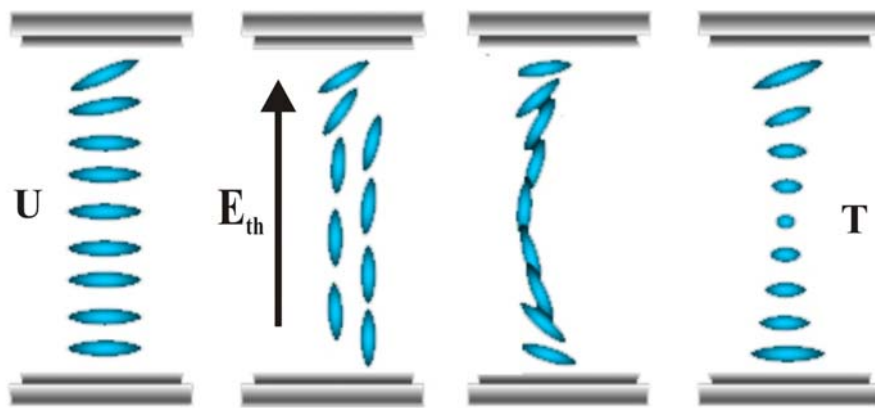


**Figure 2.10.** Texture and transition in the BiNem display.

### 2.1.5.5. Zenithal Bistable Display (ZBD)

The Zenithal Bistable Display (ZBD) uses surface gratings to achieve bistability [34, 35]. The surface is treated with an alignment layer inducing a relief grating with short pitch and deep profile. Two distinct surface states are possible: the first



state is quasi-homeotropic leading to a continuous director configuration, and the second surface state is quasi-planar, with low pre-tilt and supported by a pair of defect lines per grating period (figure 2.8). With a suitable planar anchoring on the opposite plate, the bistable states are respectively hybrid and twisted. The switching of the ZBD is based on the flexo-electric coupling with the surface polarisation under strong electric field enabling a sort of local surface anchoring breaking.

The main advantages of the ZBD are the long-term bistability and it is unaffected by mechanical or thermal perturbations. However, in practice this device requires bistable surfaces with good uniformity on a large scale.

An interesting recent development has been made by Hewlett-Packard, by using array of pits instead of gratings.

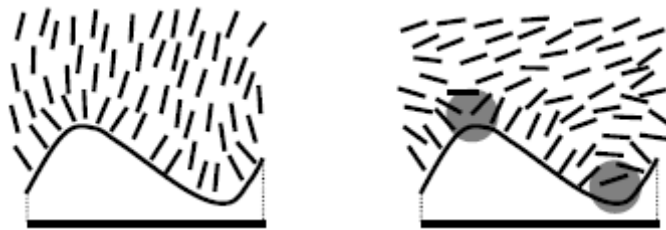


**Figure 2.11.** Textures in the zenithal bistable display.

## 2.2. A new technology: the nematic order reconstruction induced by electric field

Most available LCDs now, are using globally bistable pixels by using monostable texture changes; their bistability is not intrinsic but controlled by an active element. This is the case of the well-known active matrix displays “TFT LCDs”. The active element could be thin film transistor or diodes, one per pixel, which make the display very complex and expensive. In the above sections we summarized the most common bistable modes potentially useful for LCDs technologies with intrinsic bistability. In all previous methods, the order parameter  $S$  is fixed and the textures change, varying the rotation of the long axis of the order parameter, which is a uniaxial tensor. In this work, we propose another way to obtain transitions between two distinct textures without any surface breaking. The switching between these two topologically distinct textures can be produced by bulk order transition under strong electric fields where the spontaneous nematic order is first destroyed and then reconstructed. This uniform bulk transition is analogous to the one of the line defect core, which was first shown by Schopohl and Sluckin twenty years ago [16]. In principle, the long axis of the order tensor, which is in the ground state locally along  $x$ , can be reconstructed along  $z$  from the dielectric coupling of liquid crystal molecules, which prefer to align along  $E_z$ . The change by  $\pi/2$  of the direction of the long axis of the order tensor can happen by letting one eigenvalue grows at the expense of another until a new state is reached. In the new state, the order tensor is differently oriented and has different eigenvalues but its eigenframe remains unchanged. During the exchange of the two eigenvalues, the order tensor  $Q$  varies continuously and does not vanish implying a wealth biaxial state.

First experimental results, which seems to show such an order reconstruction was presented by Martinot Lagarde et al. [36] who presented a static biaxial melting

model. The first dynamical description of the order reconstruction has been presented by Virga et al. [37, 38], together with experimental results, qualitatively interpreted through a Landau-de Gennes-Khalatnikov one-dimensional dynamical model. Figure 2.12 describes the basic principle of a nematic liquid crystal layer of thickness  $d$  that undergoes the splay-bend transition under the action of an electric field. The layer is sandwiched between two parallel plates, and we assume that both the electric field  $E$ , and the  $z$ -axis are normal to the plane of the substrates. The transition from the quasi-splay structure to the bent one happens by applying a positive electric pulse perpendicular to the plates. For all electric fields lower than the threshold  $E_{th}$ , the nematic director  $n$  is expected to be almost everywhere parallel to the field  $E$ , except for symmetry reason in a thin layer in the center of the cell of thickness comparable to the electric coherence length itself. This wall is strongly biaxial and disappears at  $E = E_{th}$  [36-38].

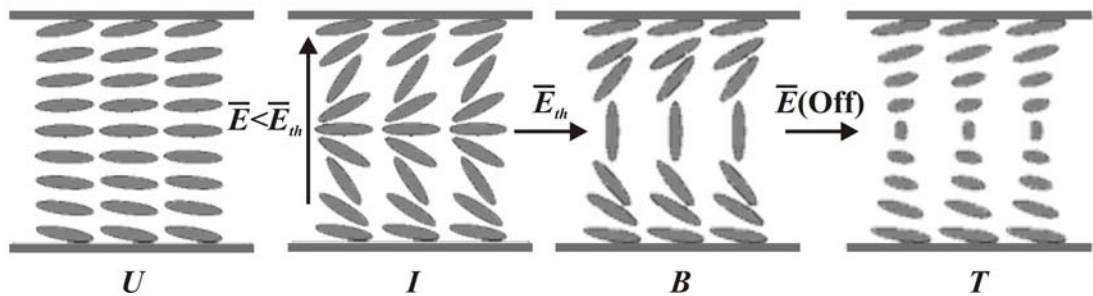


**Figure 2.12.** The transition process of the nematic order reconstruction cell. Initially the cell is in a splay state  $U$ ; if an applied field is removed below the threshold, the deformed state  $I$  returns to the splay state  $U$ . Above a threshold, the cell is in a bend state  $B$ , which is topologically distinct by  $U$ . Once  $B$  is formed, removing the applied field, it doesn't go back to  $U$ , but relaxes to a twist state  $T$  with its same topology.

# **CHAPTER III**

**~Numerical techniques~**



# Chapter 3

## Numerical techniques

Liquid crystal displays (LCDs) have been widely used for note book computers, desktop monitors and televisions. Accurate modelling and optimization are critical to design LCDs with high quality performance, which includes fast response time and wide viewing angle. Therefore, an accurate model of liquid crystal deformation is a prerequisite for reliable device design and subsequent dynamical analysis. The model presented here is based on the free energy formulation using a  $Q$ -tensor representation, and consists of the determination of the unknown coefficients of  $Q$ -tensor which minimize the free energy of the system. To solve this problem, we have used finite element method (FEM) based on Galerkin's formulation, that consists on a weak formulation of the weighted energy of the residual of the non linear equations in order to simplify the calculation routine.

### 3.1. $Q$ -tensor versus vector representation

Nematic liquid crystals are rod like molecules and most experimental phenomena are completely described by the director and the scalar order parameter that indicates the average direction of orientation of the molecules and how they are aligned along it. In practice the director varies continuously over the space. However, the transition from ordered to disordered states escapes from the

continuum theory. The classical microscopic description of defects and surface phenomena yields undesired results as well [19]. This problem was solved by de-Gennes using the order tensor theory which focuses on the orientational probability distribution, and introduces the measures of the degree of orientation and biaxiality [1, 39]. In the frame of this theory, a nematic liquid crystal can be presented as three different phases, which can be identified through their optical properties, in fact that its Fresnel ellipsoid is closely linked to the order tensor itself. In the isotropic phase the order tensor  $Q$  vanishes and optically behaves as an ordinary fluid. An uniaxial nematic has one optical axis and two eigenvalues of its order tensor coincide. Finally, in a biaxial nematic all the eigenvalues of the order tensor are distinct and the Fresnel ellipsoid possesses two optical axes.

Within the Landau-de-Gennes theory, the ground state may be either isotropic or uniaxial, depending on the external temperature. However, biaxial domains have been predicted and observed especially close to defects and external boundaries. Sluckin analyzed in detail the core of a defect and found that inside it there is a matching region where the liquid crystal is biaxial and connect the two outer topological distinct uniaxial states [19]. More recent studies show that a biaxial region inside the nematic liquid crystal can be induced by an external electric field [36-38]. In particular the transition between a splay and a bend state inside a  $\pi$ -cell can be obtained if a biaxial melting happens in the middle of the cell. This phenomenon is what we call “biaxial order reconstruction”. Such phenomenon is difficult to explore experimentally (i.e. very quick phenomenon) and it is influenced by confining geometries. Consequently, numerical computations assume a role of increasing importance in the analysis of such systems.

## 3.2. Computer simulations of physical systems

Throughout history, science has attempted to describe natural systems in terms of set of mathematical expressions. It is impressive how successful many of these mathematical constructions have been not only in describing observed events but also in predicting new results. With the fortuitous arrival of the computer, scientists and engineers have acquired a tool that is uniquely capable of performing thousands or millions of mathematical calculations while simultaneously storing equally impressive amounts of data. Generally, scientists use a structured approach for solving of physical problems: problem solving method [40]. It means that problems must be approached mathematically, applying an algorithm or step by step procedure by which one arrives at solution. The problem solving process for a computational problem is schematised in figure 3.1.

1. define the problem
2. create a mathematical model
3. develop a computational method for solving the problem
4. implement the computational method
5. test and assess the solution

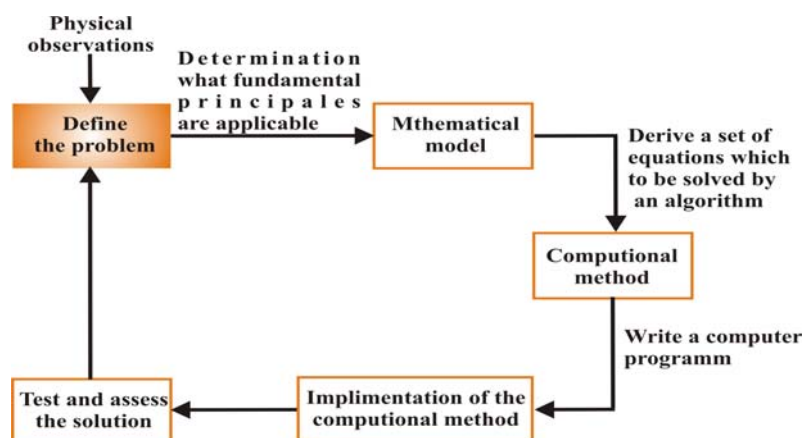


**Figure 3.1.** Problem solving approach.



Before starting any calculation, we must fully define the problem. If the problem is not defined correctly, we will, in effect, be asking the wrong question. So, we must recognise and determine what theoretical and experimental knowledge can be applied, collect all the data and information about the problem. After we have defined the problem we start to find the right mathematical description for the phenomenon to be modelled, starting with as simple as possible model including only the most essentials characters. Hence from the mathematical model identified, we must derive a set of equations that allow the calculation of the desired parameters and variables and develop an algorithm or step by step method of evaluating the equations involved in the solution. At this stage we begin to implement the computational method writing a computer program that solves the problem. The final step is to test and asset the solution. In many aspects, assessment is the most open-ended and difficult of the five steps involved. If the initial assumptions made in creating the mathematical model comes out wrong the model would be improved.

### **3.3. Modeling of the $Q$ -tensor dynamic inside a LC cell**

Modelling the dynamics of the  $Q$ -tensor inside a nematic cell in response to external electric field generally starts off with minimizing the free energy within the cell. However, awing to high nonlinearity of the free energy expression coupled with electric energies, a direct solution of the deformation of the  $Q$ -tensor and the potential distribution is quasi-impossible. Therefore, the dynamical modelling usually involves an iteration process [40]: minimizing the LC free energy to update  $Q$ -tensor profile and solving Gauss-law to update the potential profile.

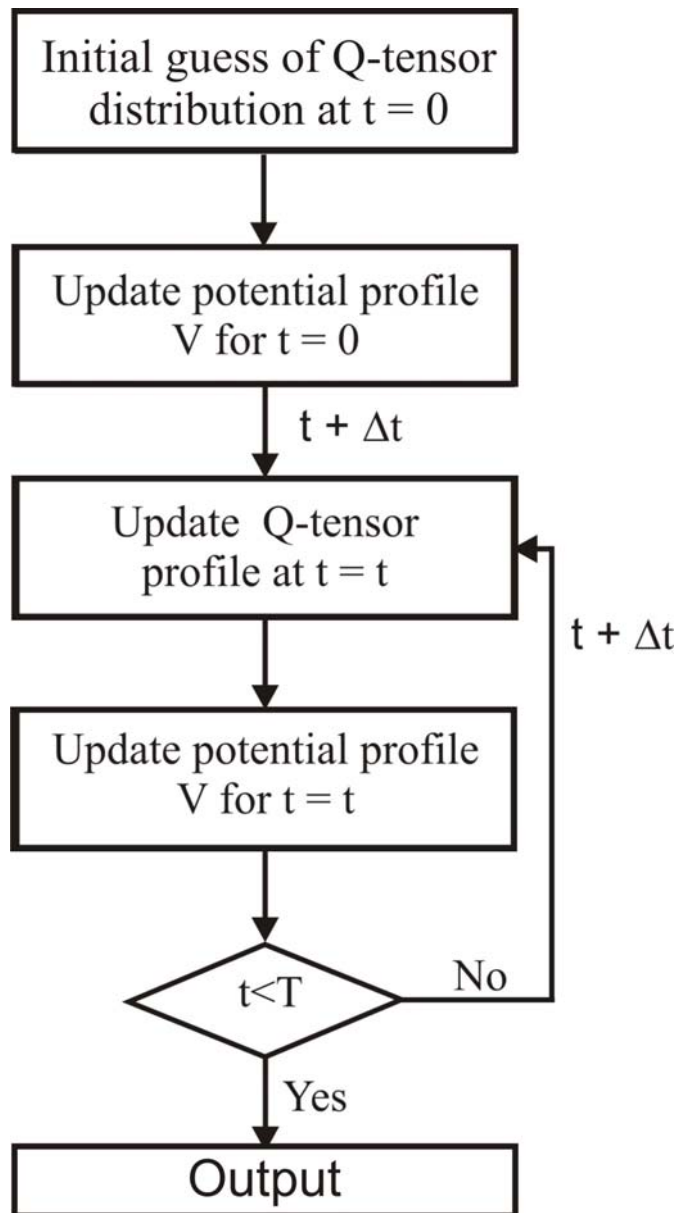


**Figure 3.2.** Flow diagram for the  $Q$ -tensor dynamical modelling.

### 3.4. $Q$ -tensor distribution update theory

As we mentioned in chapter 1 section 3, the free energy density is assumed to depend on the tensor order parameter  $Q$  and all first order differentials of  $Q$ . In addition to the elastic and electric energy terms, we need to add a temperature energy term that takes into account the material tendency to spontaneously arrange in ordered or disordered states. Basically, we can formulate the thermal energy density by using an expansion in powers of the  $Q$ -tensor in the Landau-de Gennes theory [1]:

$$F_t = a \cdot \text{tr}(Q^2) + \frac{2b}{3} \text{tr}(Q^3) + \frac{c}{2} (\text{tr}(Q^2))^2 \quad (3.1)$$

The coefficients  $a$ ,  $b$  and  $c$  are in general temperature dependent. It is, however, usual to approximate these coefficients by assuming that  $b$  and  $c$  are temperature independent while  $a = a_0 (T - T^*)$  where  $a_0 > 0$  and  $T^*$  is the supercooling temperature (the temperature at which the isotropic phase becomes completely unstable).

In general, the traceless, symmetric  $Q$ -tensor can be written in the form of a 3x3 matrix with five independent elements

$$Q = \begin{pmatrix} q_1 & q_2 & q_3 \\ q_2 & q_4 & q_5 \\ q_3 & q_5 & -q_1 - q_4 \end{pmatrix} \quad (3.2)$$

where  $q_1, q_2, q_3, q_4$  and  $q_5$  are function of  $x, y, z$  and the time  $t$ .

Numerical simulation of  $Q$ -tensor transient state at each time step under constant voltage is based on minimizing the total free energy  $F$  of the liquid crystal: the elastic energy of any distortion of the nematic material, thermotropic energy which dictates the preferred phase of the material, electric energy from an external applied electric field and surface term representing the interaction energy between the confining surface and the liquid crystal

$$F = F_d + F_t + F_e + F_s \quad (3.3)$$

$$F = \int_v \overbrace{(F_d + F_t + F_e)}^{F_b} dv + \int_s F_s dS \quad (3.4)$$

where the energies densities  $F_d, F_t$  and  $F_e$  depend on the dependent variables of the tensor order parameter.

Equation (3.4) can be written as function of the order tensor parameter  $Q$  and its all first order differentials,

$$F = \int_v F_b(q_i, \nabla q_i) dv \quad (3.5)$$

In the static case the minimization of the free energy leads to sets of five non linear coupled differential equations

$$\sum_{j=1}^3 \frac{\partial}{\partial x_j} \left( \frac{\partial F_b}{\partial q_{i,j}} \right) = \frac{\partial F_b}{\partial q_i} \quad i = 1 \dots 5 \quad \text{and} \quad q_{i,j} = \partial q_i / \partial x_j \quad (3.6)$$

when the dynamic evolution involves inclusion of a Rayleigh dissipation function [41],

$$\gamma \frac{\partial D}{\partial \dot{q}_i} = \sum_{j=1}^3 \frac{\partial}{\partial \dot{x}_j} \left( \frac{\partial F_b}{\partial q_{i,j}} \right) - \frac{\partial F_b}{\partial q_i} = - \left( - \sum_{j=1}^3 \frac{\partial}{\partial \dot{x}_j} \left( \frac{\partial F_b}{\partial q_{i,j}} \right) + \frac{\partial F_b}{\partial q_i} \right) = - [F_b]_{Q_i} \quad (3.7)$$

$$\frac{\partial D}{\partial \dot{q}_i} + \frac{1}{\gamma} [F_b]_{Q_i} = 0 \quad i = 1 \dots 5 \text{ and } \dot{q}_i = \frac{\partial q_i}{\partial t} \quad (3.8)$$

where  $D$  is the dissipation function given by

$$D = \text{tr} \left( \left( \frac{\partial Q}{\partial t} \right)^2 \right) \quad (3.9)$$

$\gamma$  is related to Leslie's rotational viscosity  $\gamma_1$  (which is  $\alpha_3 - \alpha_2$ ),

$\gamma = \gamma_1/S$  with  $S$  is the uniaxial order parameter of liquid crystal when the experimental measurement of  $\gamma_1$  was taken.

In our cell we have used strong anchoring so that, to solve the problem we have used Dirichlet boundary conditions: we fix the tensor order along the boundary substrates, simulating infinite strong anchoring.

We have used a relaxation method to solve the dynamical behaviour of the  $Q$ -tensor

$$Q_i^{t+\Delta t} = Q_i^t + \frac{\Delta t}{\gamma} [F_b]_{Q_i} \quad i = 1 \dots 5 \quad (3.10)$$

Some stability limit for the time step  $\Delta t$  exists. In general, as the spatial mesh becomes finer, the maximum stable time step becomes smaller quadratically.

### 3.5. Potential profile update theory

At given  $Q$ -tensor distribution and electrode voltage, we have to calculate the unknown electric field inside the liquid crystal. Maxwell's equations must be satisfied

$$\nabla \cdot D = 0 \quad (3.11)$$

$$\nabla \times E = 0 \quad (3.12)$$

Equation (3.12) is automatically satisfied if we choose that  $E = -\nabla U$  so we have to solve only the Gauss-law

$$\nabla D = \nabla(-\varepsilon_0 \bar{\varepsilon} \nabla U + P_f) = 0 \quad (3.13)$$

where  $\bar{D} = \varepsilon_0 \bar{\varepsilon} \bar{E} + \bar{P}_f$  and  $\bar{\varepsilon} = \Delta \varepsilon^* Q + \bar{\varepsilon} I$  with  $\Delta \varepsilon^* = (\varepsilon_{\parallel} - \varepsilon_{\perp})/S$  and  $\bar{\varepsilon} = (2\varepsilon_{\perp} + \varepsilon_{\parallel})/3$  and  $P_f$  is the spontaneous polarization.

### 3.6. FEM implementation

The high nonlinearity of equation (3.5) indicates that direct solutions of the  $Q$ -tensor and voltage profile (3.13) are difficult to obtain. However, the Galerkin's method associated to a weak formulation of the residual can bypass this difficulty of weighted residual of the differential equations [42, 43].

Suppose we divide the study region  $\Omega$  in  $M$  element regions with  $N$  nodes. The local element has a specific shape (in our case we will use or linear element in the case of 1D or triangular element in the case of 2D) and in general each element domain will have  $m$  nodes and  $m$  interpolation functions (considering first order interpolation functions) as well. In any element domain (e.g.  $e^{\text{th}}$  element) the local  $Q$ -tensor distribution can be interpolated by its  $m$  local node values using  $m$  local basis functions as

$$Q_i^e = \sum_{j=1}^m a_{ij}^e W_j^e \quad i = 1 \dots 5 \quad (3.14)$$

where  $a_i^l$  and  $W_j^l$  are the  $j^{\text{th}}$  node value and interpolation function in the  $e^{\text{th}}$  local element for the  $i$  element of the  $Q$ -tensor matrix respectively. The form of  $W_j^e$  is well defined and for a triangle element it is

$$W_j^e(x,y) = a_j^e + b_j^e x + c_j^e y \quad j = 1 \dots m \quad (3.15)$$

the  $a_j^e$ ,  $b_j^e$  and  $c_j^e$  coefficients are determined the node coordinate values and the area of each triangle.

Similarly, the residual  $R^e$  in each element domain  $\Omega^e$  can be weighted by the element basis functions as

$$\int_{\Omega^e} \left( \frac{d\tilde{Q}_i^e}{dt} + \frac{1}{\gamma} [F_b]_{Q_i^e} \right) W_j^e d\Omega^e = 0 \quad i = 1 \dots 5 \text{ and } j = 1 \dots m \quad (3.16)$$

Substituting the  $\tilde{Q}_i^e$  and expanding the above equation with the time-difference scheme leads to

$$\left( \tilde{Q}_i^e \right)^{t+\Delta t} = \left( \tilde{Q}_i^e \right)^t + [A^e]^1 (b^e) \quad i = 1 \dots 5 \quad (3.17)$$

$$A_{l,k}^e = \int_{\Omega^e} W_l^e W_k^e d\Omega^e \quad (3.18)$$

$$b_k^e = - \int_{\Omega^e} \frac{1}{\gamma} [F_b]_{Q_i^e} w_k^e d\Omega^e \quad (3.19)$$

by applying the assembling process of typical FEM procedure, we solve the five coupled non linear parabolic differential equations [44].



### 3.7. Example 1D-solution

In the one-dimensional case the system of equation (3.7) can be written in the following form,

$$\begin{pmatrix} 4\gamma & 0 & 0 & 2\gamma & 0 \\ 0 & 4\gamma & 0 & 0 & 0 \\ 0 & 0 & 4\gamma & 0 & 0 \\ 2\gamma & 0 & 0 & 4\gamma & 0 \\ 0 & 0 & 0 & 0 & 4\gamma \end{pmatrix} \cdot \frac{\partial}{\partial t} \begin{pmatrix} q_1 \\ q_2 \\ q_3 \\ q_4 \\ q_5 \end{pmatrix} + \frac{\partial}{\partial z} \begin{pmatrix} \Gamma_1 \\ \Gamma_2 \\ \Gamma_3 \\ \Gamma_4 \\ \Gamma_5 \end{pmatrix} = \begin{pmatrix} f_1 \\ f_2 \\ f_3 \\ f_4 \\ f_5 \end{pmatrix} \quad (3.20)$$

Equation (3.20) represents five nonlinear second-order partial differential equations describing the LC-device problem to be solved in term of five unknown components  $q_i$  of the tensor order parameter  $Q$ , where  $\Gamma_i$  and  $f_i$  are given by,

$$\begin{aligned}
\Gamma_1 &= -2L_1 \frac{\partial q_1}{\partial z} - (L_2 + L_3) \frac{\partial q_1}{\partial z} + 2L_6 q_1 \frac{\partial q_1}{\partial z} + 0.5L_4 q_2 + 2L_6 q_4 \frac{\partial q_1}{\partial z} - (L_1 + L_2 + L_3) \frac{\partial q_4}{\partial z} + L_6 \left( q_1 \frac{\partial q_4}{\partial z} + q_4 \frac{\partial q_4}{\partial z} \right) + \frac{e_{11}}{S} \frac{\partial U}{\partial z} \\
\Gamma_2 &= 0.5 \left( L_4 (-q_1 + q_4) + 4(-L_1 + L_6(q_1 + q_4)) \frac{\partial q_2}{\partial z} \right) \\
\Gamma_3 &= -2L_1 \frac{\partial q_3}{\partial z} - (L_2 + L_3) \frac{\partial q_3}{\partial z} + 2L_6 q_1 \frac{\partial q_3}{\partial z} + 0.5L_4 q_5 + 2L_6 \frac{\partial q_4}{\partial z} (q_1 + q_4) \\
\Gamma_4 &= -L_1 \frac{\partial q_1}{\partial z} - (L_2 + L_3) \frac{\partial q_1}{\partial z} + 2L_6 (q_1 + q_4) \frac{\partial q_1}{\partial z} + 0.5L_4 q_2 - (2L_1 + L_2 + L_3) \frac{\partial q_4}{\partial z} + 2L_6 \frac{\partial q_4}{\partial z} (q_1 + q_4) + \frac{e_{11}}{S} \frac{\partial U}{\partial z} \\
\Gamma_5 &= 0.5 \left( -L_4 q_3 + 2(2L_1 + L_2 + L_3 - 2L_6(q_1 + q_4)) \frac{\partial q_5}{\partial z} \right)
\end{aligned} \tag{3.21}$$

$$\begin{aligned}
f_1 &= L_6 \left( \frac{\partial q_1}{\partial z} \right)^2 - 2Bq_2^2 - 0.5L_4 \frac{\partial q_2}{\partial z} + L_6 \left( \frac{\partial q_2}{\partial z} \right)^2 + L_6 \left( \frac{\partial q_3}{\partial z} \right)^2 + A(-4q_1 - 2q_4) + 4Bq_1q_4 + 2Bq_4^2 + L_6 \frac{\partial q_1}{\partial z} \frac{\partial q_4}{\partial z} + L_6 \left( \frac{\partial q_4}{\partial z} \right)^2 + 2Bq_5^2 \\
&+ C(-8q_1^3 - 12q_1^2q_4 + q_1(-8q_2^2 - 8q_3^2 - 12q_4^2 - 8q_5^2) + q_4(-4q_2^2 - 4q_3^2 - 4q_4^2 - 4q_5^2)) + L_6 \left( \frac{\partial q_5}{\partial z} \right)^2 - \frac{\varepsilon_0 \Delta \varepsilon}{S} \frac{\partial U}{\partial z} \\
f_2 &= 0.5L_4 \left( \frac{\partial q_1}{\partial z} + \frac{\partial q_4}{\partial z} \right) - 4(Aq_2 + B(q_1q_2 + q_2q_4 + q_3q_5) + 2Cq_2(q_1^2 + q_2^2 + q_3^2 + q_1q_4 + q_4^2 + q_5^2)) \quad (3.22) \\
f_3 &= 0.5 \left( -L_4 \frac{\partial q_5}{\partial z} - 8Aq_3 + 8Bq_3q_4 - 8Bq_2q_5 - 16Cq_3(q_1^2 + q_2^2 + q_3^2 + q_4^2 + q_5^2 + q_1q_4) \right) \\
f_4 &= -4C \left( \frac{\partial q_1}{\partial z} \right)^3 - L_6 \left( \frac{\partial q_1}{\partial z} \right)^2 - 4Cq_1q_2^2 + 0.5L_4 \frac{\partial q_2}{\partial z} + L_6 \left( \frac{\partial q_2}{\partial z} \right)^2 - 2A(q_1 - 2q_4) - 4Cq_1q_3^2 + L_6 \left( \frac{\partial q_3}{\partial z} \right)^2 - 12Cq_4q_1^2 - 8Cq_2^2q_4 \\
&+ 2C(4q_3^2q_4 - 4q_4^3 - 6q_4^2q_1 - 2q_5^2q_1 - 4q_4q_5^2) + L_6 \frac{\partial q_1}{\partial z} \frac{\partial q_4}{\partial z} + L_6 \left( \left( \frac{\partial q_4}{\partial z} \right)^2 + \left( \frac{\partial q_5}{\partial z} \right)^2 \right) + 2B(q_1^2 - q_2^2 + q_3^2 + 2q_1q_4) - \frac{0.5\varepsilon_0 \Delta \varepsilon}{S} \left( \frac{\partial U}{\partial z} \right)^2 \\
f_5 &= 0.5L_4 \frac{\partial q_3}{\partial z} + B(-L_4(-4q_2q_3 + 4q_1q_5) - 4q_5(A + 2C(q_1^2 + q_2^2 + q_3^2 + q_4^2 + q_5^2 + q_1q_4)))
\end{aligned}$$

The system of equations (3.21) and (3.22) shows five coupled non-linear parabolic partial integro-differential equations.

To numerically solve the governing equations (3.13) and (3.20), we used FEM method with adaptive mesh solver with an explicit time step. For the equilibrium state, the  $Q$ -tensor elements and voltage in each grid should be recalculated in every time step until they exhibit stable response. Dirichlet boundary conditions for the order tensor on the surface is imposed which corresponds to infinitely strong anchoring. Typical calculation parameters have been chosen to give us the possibility to compare our model with the experimental evidences, different parameter values can be obtained from the literature for 5CB [45]. Moreover, the temperature dependence of the elastic constants is taken into account [46] and the scalar order parameter  $S$  is evaluated by calculating the minimum of the Landau-de Gennes energy [1]. Figures 3.4 show the director profile during the splay bend transition for cell with thickness of  $1\mu\text{m}$  and the applied voltage was turned off after  $150\mu\text{s}$ . In figures 3.4.a-d we calculated the dynamic director configuration as a function of the time for cell with pre-tilt angle fixed at  $+1^\circ$  on the top substrate and  $-1^\circ$  at the bottom substrate. We started the system in the splay state and applied  $12\text{V}$  at time  $t = 0$ . At  $t = 75\mu\text{s}$  the transition happened and at  $t_1 = 85\mu\text{s}$  all the splay configuration is transformed to the bend state which is topologically inequivalent. In figure 3.5.a we calculate the order parameter  $S = 1.5 (\text{tr}(Q \cdot Q))^{0.5}$  [47] during the transition inside the cell. As we mentioned before, when all eigenvalues of  $Q$  are distinct, the liquid crystal in biaxial state. According to [48], the degree of biaxiality of  $Q$  can be defined as,

$$\beta = \left( 1 - 6 \frac{(\text{tr} Q^3)^2}{(\text{tr} Q^2)^3} \right)^{0.5} \quad (3.23)$$

In figure 3.5.b we show the typical dynamics when a high enough electric field is applied to the cell, the transition in the centre becomes purely biaxial with  $\beta = 1$  is reached. The order tensor in the centre didn't rotate, but two of its eigenvalues are exchanged as we can see in figure 3.5.c.

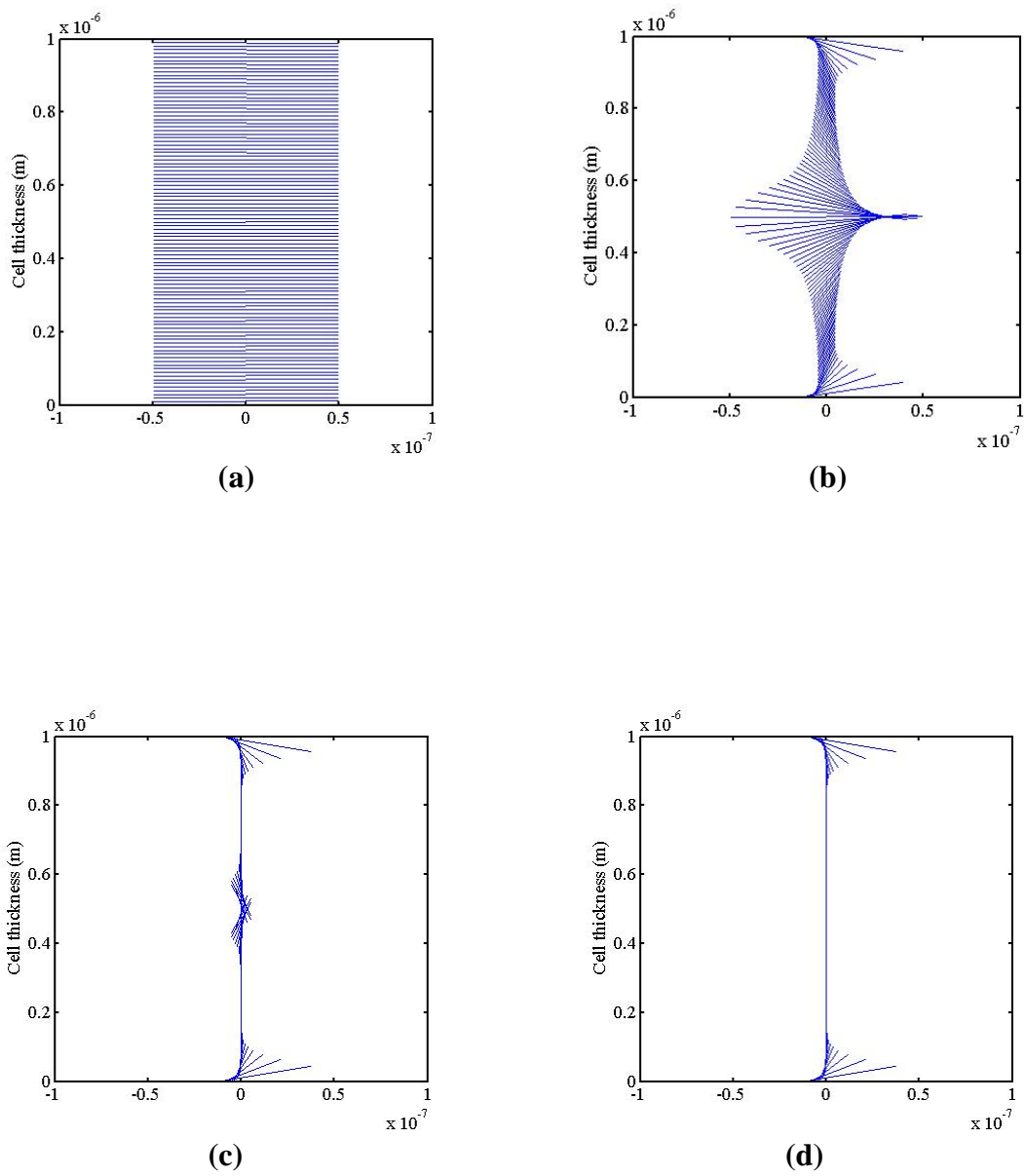
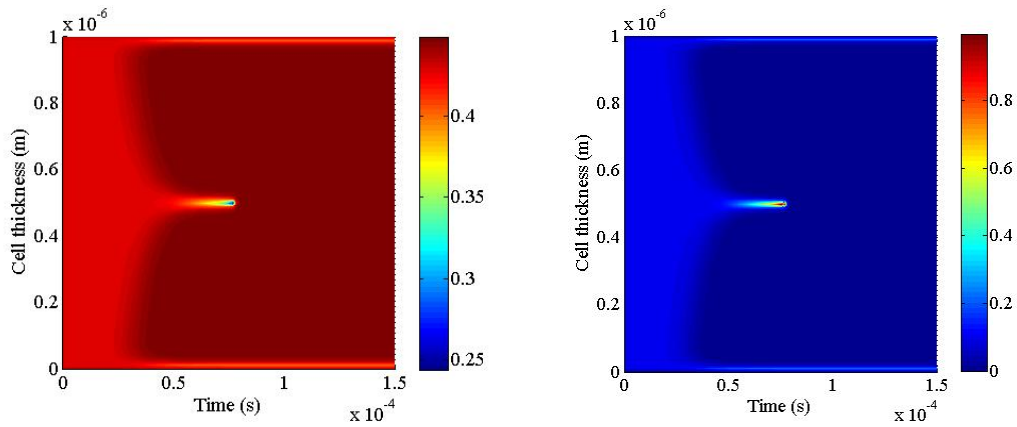
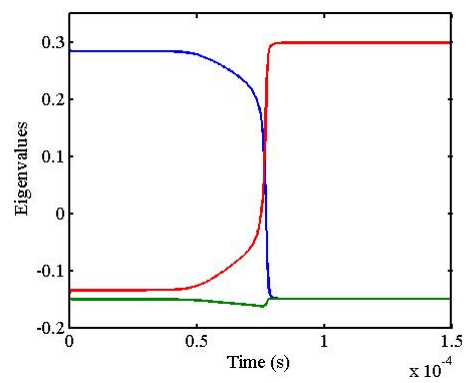


**Figure 3.3.** One-dimensional director calculations for modelling the order reconstruction: (a) at 0V,  $t = 0$  (b) at 12V,  $t = 50\mu\text{s}$  (c) at 12V,  $t = 82\mu\text{s}$  (d) at 12V,  $t = 100\mu\text{s}$ .



(a)

(b)



(c)

**Figure 3.4.** Calculated dynamic behaviours of (a) order parameter  $S$  (b) biaxiality  $\beta$  and (c) the eigenvalues of the  $Q$ -tensor.



# **CHAPTER IV**

**~~Experimental techniques~~**





# Chapter 4

## Experimental techniques

In the coming chapters, we show experimental results of our investigations on the electric field induced order reconstruction in nematic cells. The main experimental investigations are performed using electro-optical characterisations. In this chapter we explain the principles of cells construction and the experimental setup used for our investigations. The first paragraph focuses on the preparation of our samples (cells), we then present samples properties characterizations and finally we show the experimental setup used to perform the measurements reported in the next chapters.

### 4.1. Cells construction

To fabricate our cell, we first cut a sheet of glass already covered with ITO (Indium Tin Oxide) film into whatever size desired. The photolithography process takes place. The glass pieces (20x15x1 mm) are then cleaned with NaOH solutions using a brush and then rinsed with distilled water. After this process is finished, they are put in a Petri capsule filled with NaOH solution and placed in an ultrasonic cleaner for 15 minutes. Hence the glass is taken out and rinsed with

distilled water, with acetone finally with distilled water, and dried making very sure to get all the water off. The glass is now clean with patterned ITO. The liquid crystal alignment is achieved either by spin coating a polymer layer or evaporating  $\text{SiO}_x$  film. Different polymer aligning materials are used: polyvinyl alcohol (PVA) dissolved in water, polyimide (LQ1800 by Hitachi Chemical) (PI) dissolved in 1-methyl-2-pyrrolidinone. After spin coating, the desired film is baked in the oven at right temperature and the required time depending on the polymer used. The polyvinyl alcohol requires thermal baking step of 1h at  $120^\circ\text{C}$ . The thickness of the polyimide LQ1800 (PI) layer was varied by changing the concentration of the solvent and then cured by two thermal baking steps: 1h at  $140^\circ\text{C}$ , followed by 1h at  $250^\circ\text{C}$ . The surfaces of the PVA or polyimide coated substrates are then rubbed in one direction by a rotating cylinder covered with a rubbing cloth (figure 4.1). At this point, we are now ready to assemble the cell: the two glass plates are glued together under pressure with drops of UV curable glue mixed with calibrated spherical spacers of  $1.9\ \mu\text{m}$  diameter, deposited outside the pixel area. Looking at the cell under monochromatic light, if any fringes can be seen, they are probably caused by cell non-uniformity. The measurement of the cell thickness is based on an optical interference method; in any case the cell thickness corresponds to the sphere diameter within 5%. Now we have an empty cell ready to use. The cell is then filled by capillarity with isotropic 5CB liquid crystal at  $40^\circ\text{C}$  in a vacuum chamber.

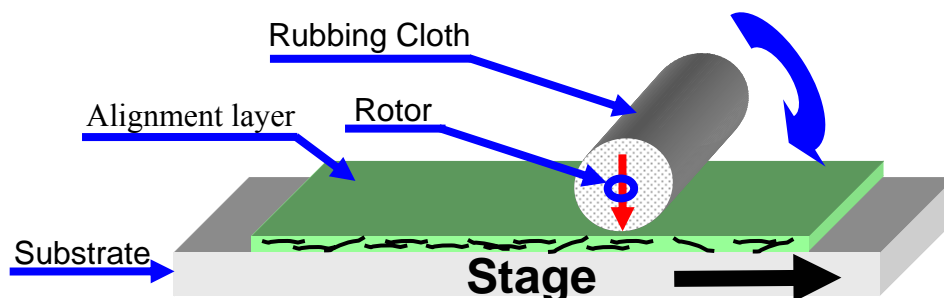


**Figure 4.1.** Stretching of the film surface by rubbing.

## 4.2. Surface characterization

In this paragraph we present preliminary analysis of surface of our cells in order to evaluate the effect of surface treatment on electro-optic measurements. So, we describe a simple experimental method used to determine the pre-tilt angle of the nematic on the surface  $\theta_s$  and the polar anchoring strength  $W_0$ . The zenithal angle (pre-tilt) was measured by means of an interferential method (crystal rotation) [49], with uniform-shaped (equal thickness) cells and made with anti-parallel alignment on both alignment layers (figure 4.4). The use of anti-parallel aligned cells is necessary for uniform orientation of the nematic and essential for a correct determination of the zenithal anchoring orientation. The method is based on the measurement of the optical phase difference  $\Gamma$  of a liquid crystal cell with thickness  $d$  as a function of the angle formed by the beam and the normal to the cell plane. In figure 4.2 a block diagram is shown of the experimental setup. A beam laser ( $\lambda = 632$  nm) is divided by a semi-silvered mirror into two beams, the signal and the reference. The signal beam is linearly polarized by a polarizer at  $45^\circ$  with respect to the vertical axis, passes through the sample (which transforms the polarization state from linear to elliptical) and then through a quarter wave ( $\lambda/4$ ) plate (with its optical axis at  $45^\circ$ ) which transforms the elliptical polarization state back into linear one with a rotation of the plane of polarization equal to  $\Gamma$ . The out coming signal from the ( $\lambda/4$ ) plate is chopped by a rotating analyzer (rotation frequency 90 Hz) and detected by a photodiode which delivers to a lock-in. The reference beam is also polarized linearly in the same direction and chopped by the same rotating analyser and then detected and delivered to the lock-in by means a second photodiode. The experimental optical path difference measured for a scan of incidence angle  $\varphi$  from  $-30^\circ$  to  $30^\circ$  is fitted by the equation (4.1) using  $d$  and  $\theta_s$  as unknown variables [49].

$$\Gamma = \frac{2\pi d}{\lambda} \left\{ \frac{n_o^2 - n_e^2}{n^2} \sin(\theta_s) \cos(\theta_s) \sin(\varphi) + \frac{n_o n_e}{n^2} \sqrt{n^2 - \sin^2(\varphi)} - \sqrt{n_o^2 - \sin^2(\varphi)} \right\} \quad (4.1)$$

$$n^2 = n_o^2 \cos^2(\theta_s) + n_e^2 \sin^2(\theta_s)$$

Where  $n_o$  and  $n_e$  are respectively the ordinary and extraordinary optical refraction index of light,  $\theta_s$  is the pre-tilt angle,  $d$  the cell thickness and  $\varphi$  the incidence angle. A typical example of the results is shown in figure 4.3.

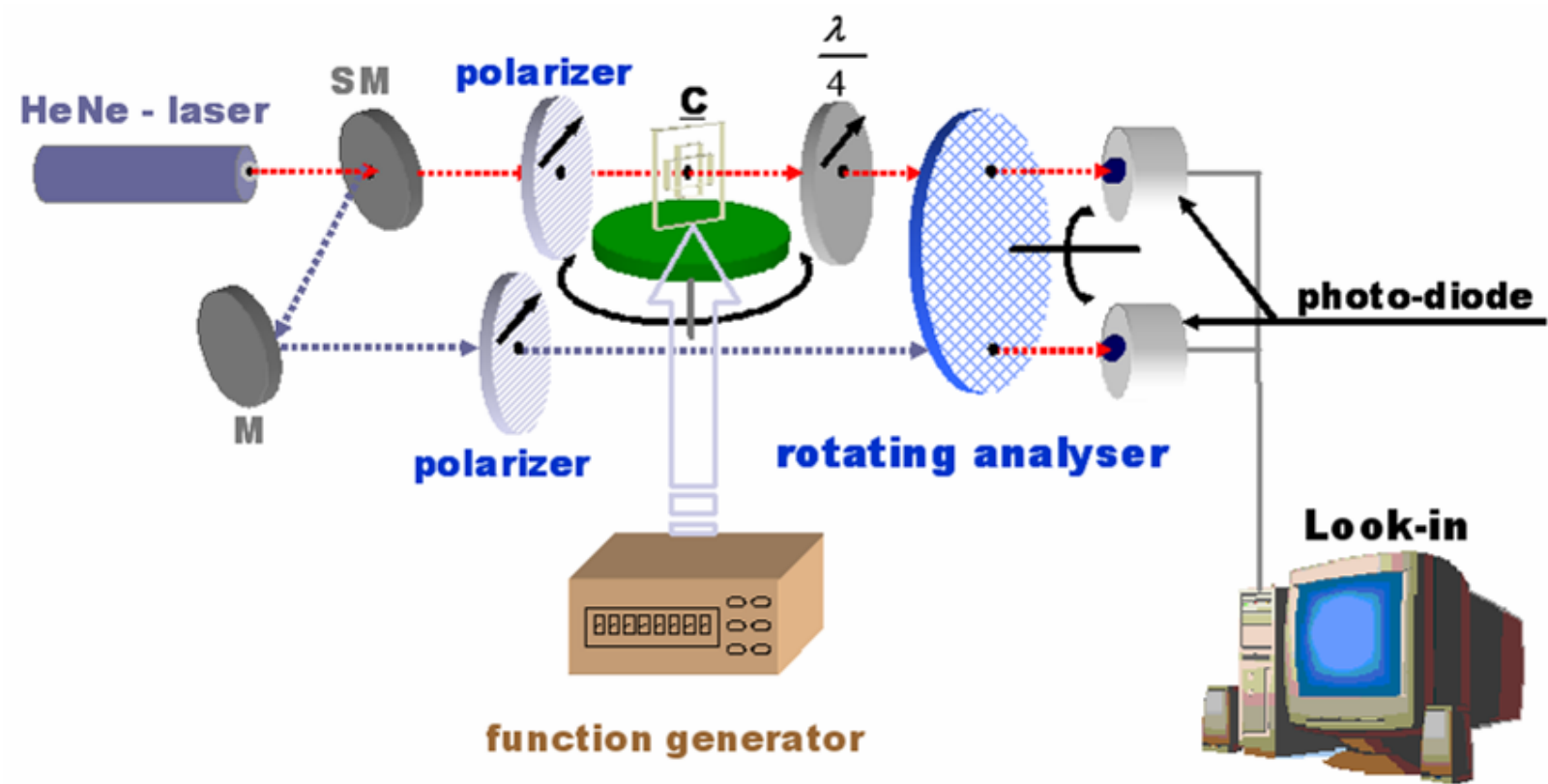


**Figure 4.2.** Experimental set up used for pre-tilt angle and anchoring strength measurements.

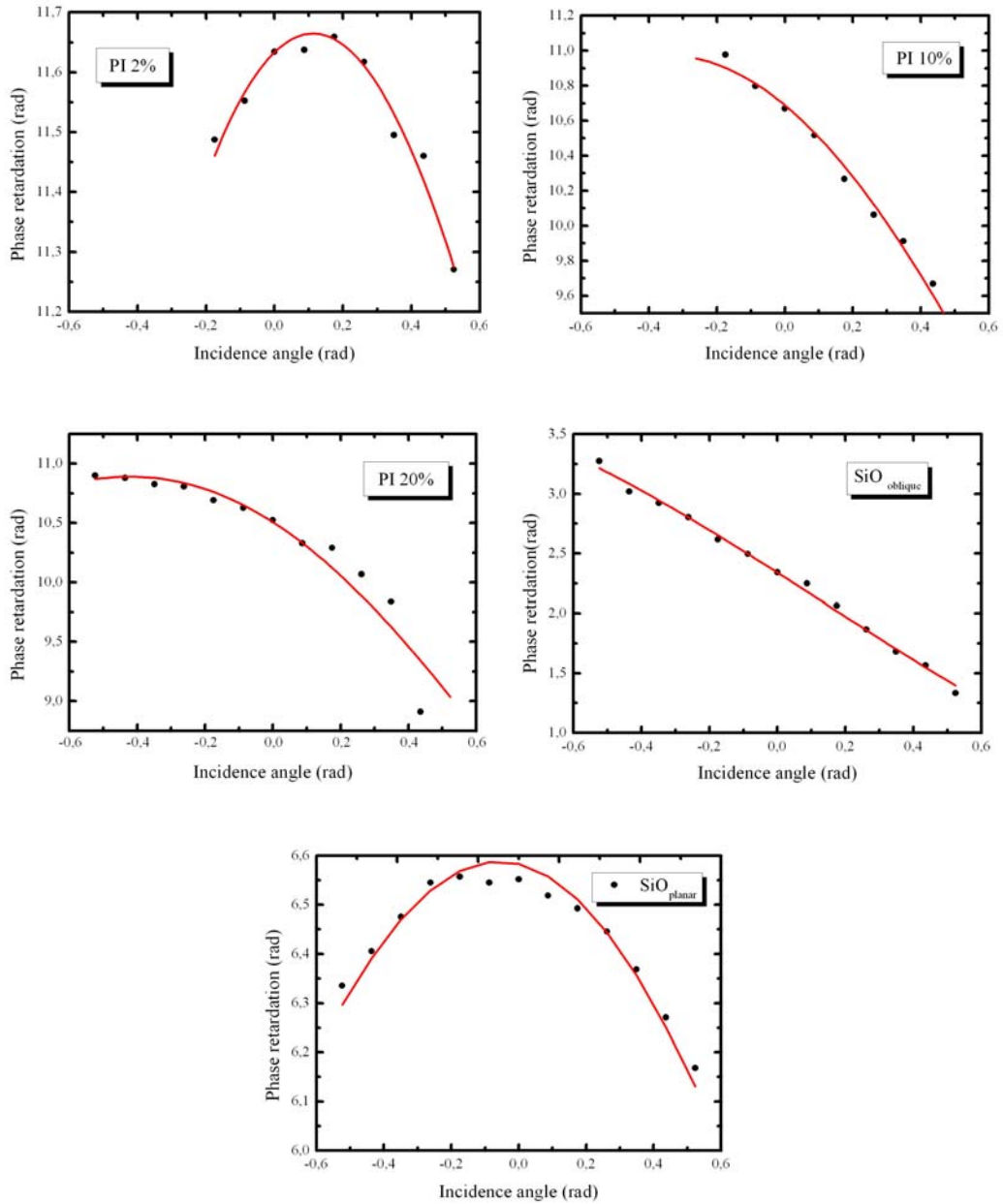


**Figure 4.3.** Phase retardation as a function of the rotation angle. The red line is the best fit of the experimental data using equation 4.1.

We now describe the experiment performed in order to study the zenithal anchoring strength and we start by describing a simple model used to the zenithal extrapolation length. The method is based on the determination of the zenithal extrapolation length from measurements of the director distortion when subjected to an external electric field. A hybrid cell (figure 4.4) is used because it allows a number of simplifying assumptions in the model used to fit the experimental data. The model is used to calculate the cell retardation. By varying the model parameters, the best fit to the experimental data give us the anchoring strength. The optical retardation may be given by the following equation [50]:

$$\delta(V) = n_o \int_0^d \left\{ \frac{1}{\sqrt{1 - R_0 \sin^2(\theta(z, V))}} \right\} dz \quad (4.2)$$

where  $R_0 = 1 - \left( \frac{n_o}{n_e} \right)^2$

We used the experimental set up already described above. We measured the retardation as a function of the applied voltage (an AC sine voltage of 1 KHz). A typical set of experimental data fitted by equation (4.2), for the planar anchoring case are shown in figure 4.5. The experimental results of the pre-tilt angle and anchoring strength are presented in table 4.1.



**Figure 4.4.** Geometry of anti-parallel and hybrid cell respectively.



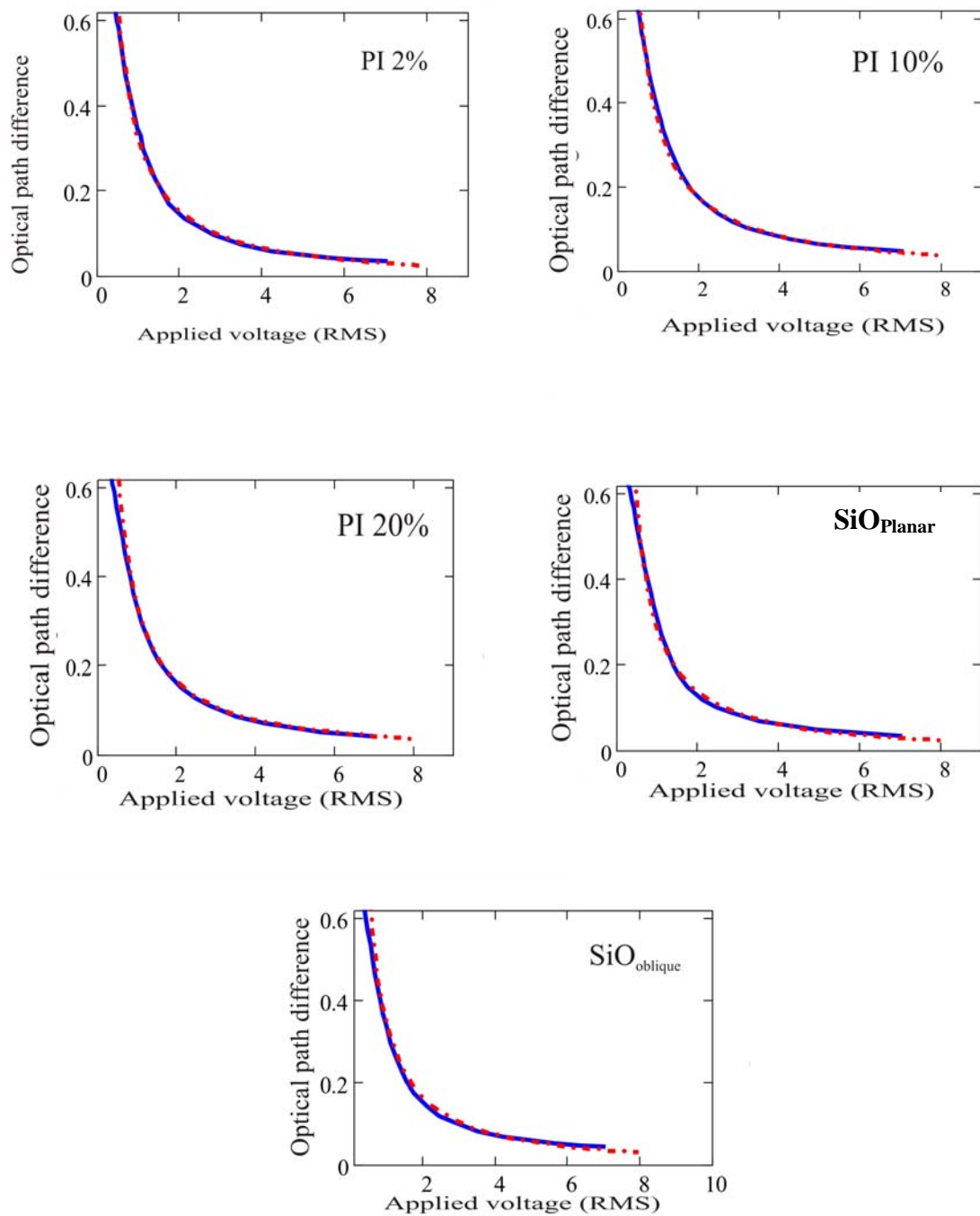


**Figure 4.5.** Typical optical path difference as a function of the applied voltage. The red dash dot line is the best fit of the experimental data using equation 4.2.

	PI2%	PI10%	PI20%	SiO <sub>o</sub>	SiO <sub>p</sub>
$\theta_s$ (°)	2.0±0.2	6.0±0.4	8.0±0.4	29.0±0.8	0.4±0.2
$W_s \cdot 10^{-4}$ (J/m <sup>2</sup> )	1.0±0.2	2.0±0.4	2.5±0.6	1.5±0.1	1.0±0.1

**Table 4.1.** Experimental results obtained for the pre-tilt angle and the anchoring strength on the different substrates under study.

### 4.3. Electro-optical setup

Certain materials change their optical properties when subjected to an electric field. This is caused by forces that distort the positions, orientations, or shapes of the molecules constituting the material. The electro-optic effect is the change in the refractive index resulting from the application of a dc, ac or low-frequency electric field. An electric or magnetic field applied to an anisotropic electro-optic material modifies its refractive indices and thereby its effect on polarized light (figure 4.6).

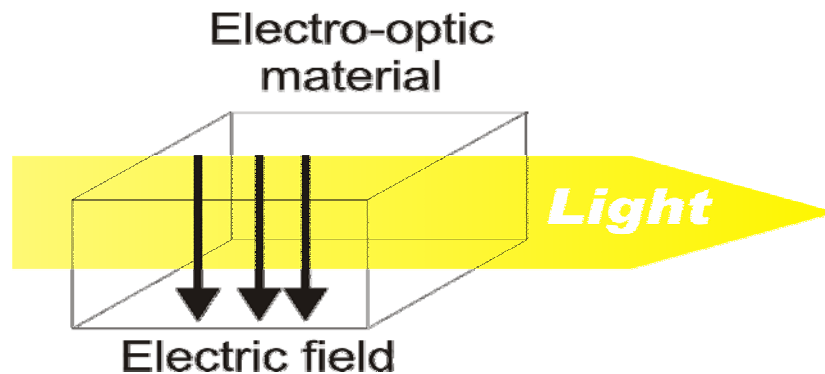


**Figure 4.6.** An electric field applied to electro-optic material changes its optical properties. The electric field therefore controls the light.

This work is devoted to the electro-optic properties of liquid crystals and in particular nematic. As mentioned in section 1.2 an electric field applied to the molecules of liquid crystal causes them to alter their orientations. This leads to changes in the optical properties of the medium, i.e. it exhibits an electro-optic effect. This behaviour is the basis of most liquid crystal display devices. A schematic illustration of the experimental set up used to investigate the electric field induced order reconstruction in nematic cells is shown in figure 4.8. The cell is situated between crossed polarizers under polarizing microscope brand Leica DMRX. An isotropically liquid phase does not affect the light and, therefore, no light can cross the analyzer. In the case of liquid crystalline phase, however, the birefringent property of the material induces refraction of the light according to the director orientation. Since only the component of the refracted light parallel to the analyzer polarization direction is transmitted, the intensity of the transmitted light varies from white if  $(n.p) = 0$  to black if  $(n.p) = 1$  where  $p$  is the polarization direction of the analyser. The plate of the microscope is rotated to align the nematic director at  $45^\circ$  with respect to the optical axis of the crossed polarizers. In fact, this is the well known condition of maximum intensity for the transmitted light in presence of a birefringent sample. The transmitted light intensity can be measured by means a photomultiplier Leica Wetzlar MPV-COMBI and we can record the observed pictures of the texture changes by means of a video camera connected to the polarizing microscope. The sample is connected to Hewlett Packard pulse generator who can provide positive electric pulses (figure 4.7) whose amplitude can vary between 0.3V and 100V for pulse width in the range  $25ns-10ms$ . To measure the electric current flowing across the cell during the pulses application, the cell was connected in series to an external electric resistance  $5K\Omega$ . We measure the current from the voltage across the resistor which is detected by means of digital oscilloscope (Agilent infinium 54830D MSO 1GHz, 4GSa/s). We perform synchronous acquisitions of the electric current across the cell during the application of the electric field. The electric current data and the transmitted light intensity are acquired by a PC connected via a GPIB

interface. To study the temperature dependence of the nematic order reconstruction behaviour, the cell was placed in hot stage made InsTec with temperature resolution better than  $0.1^{\circ}\text{C}$ .

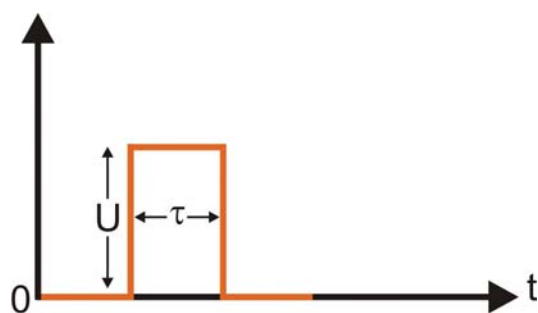


**Figure 4.7.** The signal shape used to drive the transition in our experimental cell.

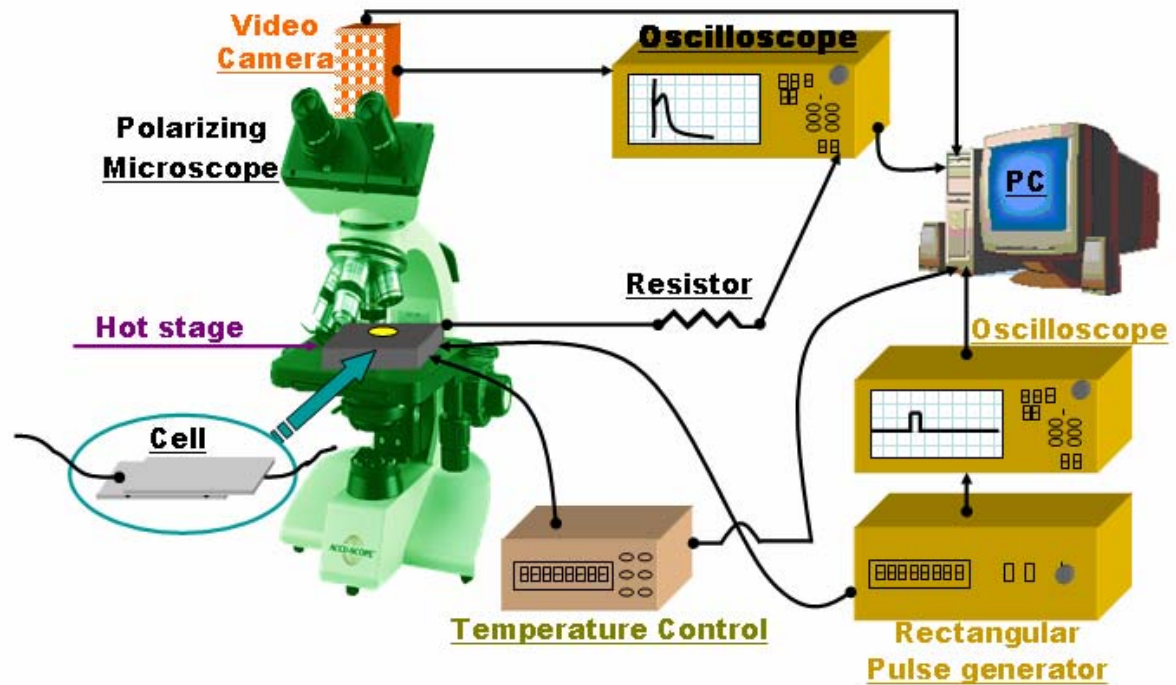


**Figure 4.8.** Electro-optic set-up. The samples is placed between crossed polarizes under polarizing microscope and when the electric field is applied to the cell, the dynamical response is detected by means of an oscilloscope.

## 4.4. Liquid crystal material

We have performed the measurements using 4-cyano-4'-n-pentylbiphenyl liquid crystal; brand K15 from Merck, (also well known as 5CB). This compound exhibit cyano-biphenyl groups with strong positive dielectric anisotropy, which gives it a strong coupling to the applied electric field. Moreover, it is robust molecule, which makes it a good candidate for the electro-optic studies, but also for the display applications. The 5CB exhibits the nematic liquid crystal phase at room temperature, the nematic-isotropic transition arises at  $T_{N-I} \approx 35^{\circ}\text{C}$  [45].

We have also used mixtures of 5CB doped with materials which can arise or decrease the biaxial tendency of the mixture.

We always introduce the nematic liquid crystal in the sample cell at a temperature of  $5^{\circ}\text{C}$  above the nematic-isotropic transition in order to eliminate all surface memory effects. The cell is then cooled down with a slow temperature variation near the nematic isotropic transition, in order to obtain a uniform orientation of the liquid crystal.

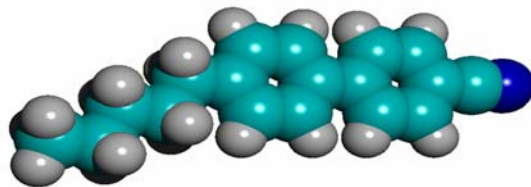


**Figure 4.9.** The molecular structure of 5CB.

## 4.5. Typical optical observations

We describe a typical experiment for a symmetric cell of thickness about  $2\mu\text{m}$ . The oblique symmetrical anchoring on the two boundary plates is obtained by polymeric (PI20%) coating, this results in a strong anchoring a small pre-tilt angle of  $8^\circ$ . The cell then is filled with the 5CB liquid crystal as described before. To observe textural changes we place the cell between crossed polarizers at a controlled angle with respect to the surface alignment direction, using a polarizing optical microscope. We fix the temperature at  $T = T_c - 1.5^\circ\text{C}$  and we choose  $1\text{ms}$  as electric pulse width. We increase slowly the applied electric field, up to  $5.1\text{V}/\mu\text{m}$  we observe just a transit optical effect. The cell birefringence is measured during the pulse from the light transmission. Upon rotating the sample, we observe a modulation in the small residual birefringence; classically, this is interpreted as an almost complete alignment of the nematic director along the electric field direction. By verifying that some transient transmitted light remains, we prove the existence of thin birefringent wall inside the cell, as expected. After the pulse, the distorted texture relaxes towards the initial planar one, with a typical curvature-controlled relaxation time of about  $4\text{ms}$ .

Increasing again slightly the applied electric field, at  $5.3\text{V}/\mu\text{m}$  we observe the onset of bright spots, at  $5.75\text{V}/\mu\text{m}$ , the whole pixel becomes uniformly bright which corresponds to the  $I$  to  $B$  transition (see figure 2.12 chapter 2). After the pulse, the bright texture relaxes back to the initial state by means of slow motion of disclination lines within a few within a few seconds. We send now electric pulses of the same amplitude at a low rate of 1 every 5 seconds to reproduce regularly the new texture to analyze. Rotating only the analyzer by about  $35^\circ$ , the new transient texture becomes black; the initial planar texture is now bright. Rotating the sample, this black is more or less independent of the absolute sample rotation, whereas the outside planar texture presents a classical periodic dark and bright aspects. This indicates that the new created texture presents rotatory power,

which is typical of a twisted texture. These optical properties are in fact the same as the ones of  $\pi$ -twisted cells obtained when breaking a weak planar anchoring on SiO [57].





# **CHAPTER V**

**~Results and discussion~**



# Chapter 5

## Results and discussion

In this chapter we present experimental results supported by numerical and phenomenological models. We start by a brief summary of previous experimental and theoretical studies of the nematic order reconstruction induced by high electric field. An improved numerical model is then compared with previous experimental results and our new experimental data. We also discuss the influence of alignment layers on the nematic order reconstruction. We start by studying the case of symmetric cells geometry where surface effects seems to be not relevant. Then we study asymmetric cells where the order reconstruction takes place close to a surface. We finally demonstrate that the anchoring breaking is a particular case of surface order reconstruction.

### **5.1. First investigations on the electric field induced order reconstruction**

During the last three years, the research in nematic electro-optics has been strongly stimulated by the demonstration of fast coherent switching between two topologically distinct textures by means of the electrically controlled nematic order reconstruction. This transition, whose effects could have been experimentally observed long time ago [51], has been correctly interpreted for the

first time by Martinot-Lagarde et al. [36], who presented a static biaxial melting model. The first dynamical description of the biaxial order reconstruction was proposed in reference [37], together with experimental results, qualitatively interpreted through a Landau-de Gennes-Khalatnikov one-dimensional dynamical model. Figure 5.1 shows the experimental order reconstruction threshold data as a function of rectangular pulse duration compared with the numerical results obtained by the model proposed by E. Virga et al. in ref. [37] close to the nematic isotropic transition. The proposed model [37] shows the same general behaviour of the experimental data, but the theoretical estimation is higher than the experimental values. In particular for longer pulse durations, the discrepancy is about a factor 2. Figure 5.2.a shows the typical behaviour of the calculated electric current flowing through the cell during the pulse application above the order reconstruction threshold [37]. The current signal shows two well defined peaks, the faster one comes from the molecular reorientation along the field of the two layers around the biaxial wall and the slower peak is created during the biaxial wall breaking [37-38]. Recently, the time resolved experimental analysis of the nematic order reconstruction has been presented by using electric current measurements coupled with texture transformation observation [38]. Figure 5.2.b presents the time dependence of the experimental current observed for applied electric field above the threshold during the biaxial transition.

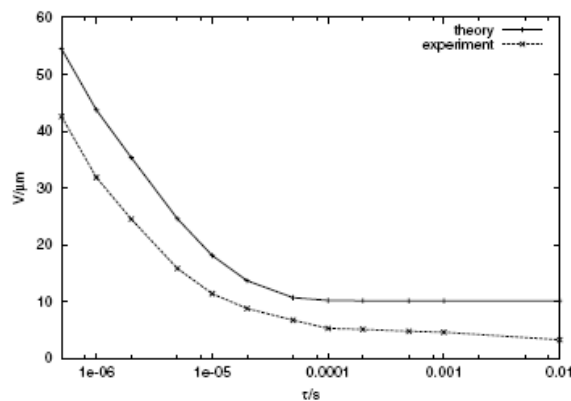


**Figure 5.1.** Experimental results compared with the theoretical model presented in reference [37].

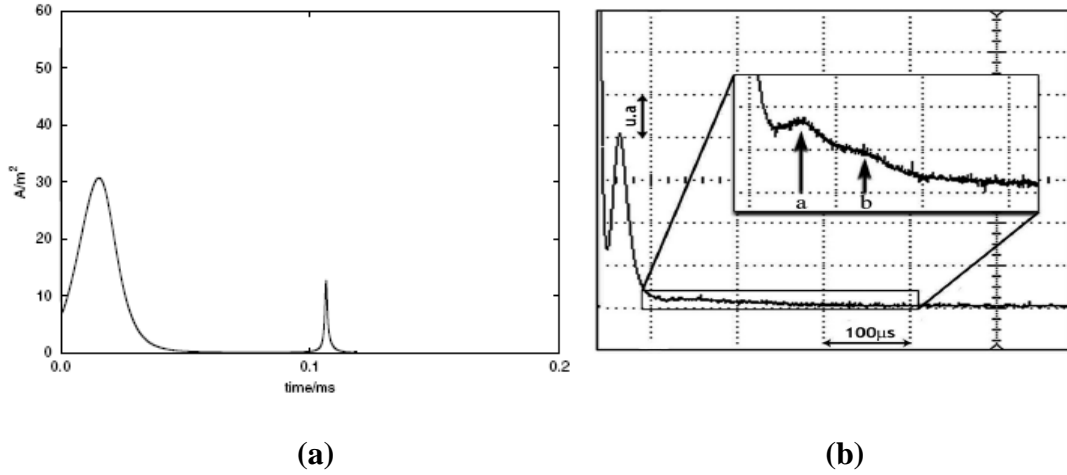


**Figure 5.2.** (a) Electric current calculated by using the model presented by Virga et al. in [37]. (b) Experimental electric current shown the order reconstruction peak [38]. In this picture the faster and larger peak is due to the usual dielectric molecular reorientation, the peak *a* is due to the nematic order reconstruction and the last peak *b* is due to ions.

## 5.2. Nematic order reconstruction in symmetric cells

### 5.2.1. Typical observations

The simplest experimental geometry to investigate the nematic order reconstruction is a cell with a nematic splay texture symmetric with respect to its middle plane. We consider a homogenous cell of nematic liquid crystal

sandwiched between two transparent indium tin oxide (ITO) coated glass plates with about 2  $\mu\text{m}$  cell gap thickness. On each plate there are two electrically conductive stripes of 1 mm width, made by photolithography on the ITO film. The two stripes are crossed to make one pixel of about 1  $\text{mm}^2$  area. The glass substrates are coated with rubbed polyimide (LQ1800) such that the nematic directors on both surfaces are anchored with a pre-tilt angle of a few degrees ( $\sim 0^\circ$  to  $10^\circ$ ). We used three sets of cells where the boundary properties were varied by changing the concentration weight 2% (SC3), 10% (SC2) and 20% (SC1) of the polyimide solution and the thin surface film is deposited by spin coating. Full descriptions of cell preparation are presented in chapter 4, section 1. The three cells are filled with the liquid crystal 5CB (Merck) and are connected to a rectangular voltage pulse generator. We can adjust independently the voltage amplitude  $U$  and the duration  $\tau$  of each electric pulse, manually triggered. In order to study the bistable behavior of our cells, we used the same experimental setup and methods already described in chapter 4. We present in figure 5.3 the dependence of the observed order reconstruction threshold  $E_{th} = V_{th}/d$  as a function of the temperature at fixed pulse duration  $\tau = 1\text{ms}$  and  $0.1\text{ms}$  for the cell SC1 and  $\tau = 1\text{ms}$  for all three cells SC1, SC2 and SC3. We can see that  $E_{th}$  decreases and tends to zero by increasing the temperature. These experimental data are fitted by a simple power law,  $E_{th} \propto (T_c - T)^\alpha$  given  $\alpha = 0.39$  for  $\tau = 1\text{ms}$  and  $\alpha = 0.38$  for  $\tau = 0.1\text{ms}$  for the cell SC1,  $\alpha = 0.40$  and  $\alpha = 0.36$  for SC2 and SC3 respectively. In the following, for all samples, we observe  $0.36 < \alpha < 0.40$ , indicating a quite similar dynamics for all cells.

These results are surprising, because they suggest a quite relevant boundary influence for the nematic order reconstruction, which in a symmetric cells should be a pure bulk phenomenon.

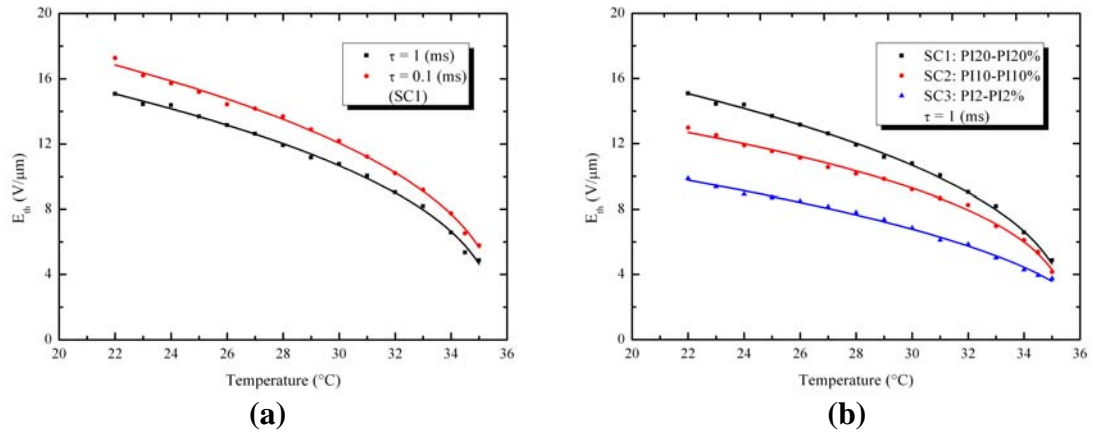


**Figure 5.3.** Temperature dependence of the threshold: (a) for the cell SC1 at two different pulse durations. (b) For three different cells SC1, SC2 and SC3 for  $\tau = 1$  ms. The fitting curves represent the power law  $E_{th} \propto (T_c - T)^\alpha$ .

### 5.2.2. Order reconstruction dynamics

Figure 5.4.a shows a typical plot of the order reconstruction threshold  $E_{th}$  versus the applied pulse duration  $\tau$  at reduced temperatures  $T_c - T = 5.2$  °C. The experimental data of figure 5.4 shows behaviours similar to the experimental observations reported in the previous figure 5.1 [37]. Also in this case by looking at the figure 5.4.a, we can distinguish three curves corresponding to three cells having three different surface treatments. We first note that, as expected, the transition thresholds increase when the pulse duration decreases, but also that, although the trend is similar, the transition thresholds for each cell depends on the PI concentration. For SC1 we observe the highest thresholds, while the lowest ones are for SC3. A typical plots of the order reconstruction threshold  $E_{th}$  versus the pulse width  $\tau$  for different temperature is shown in figure 5.4.b, c, d. In all cases  $E_{th}$  increases by decreasing the pulse duration  $\tau$ .



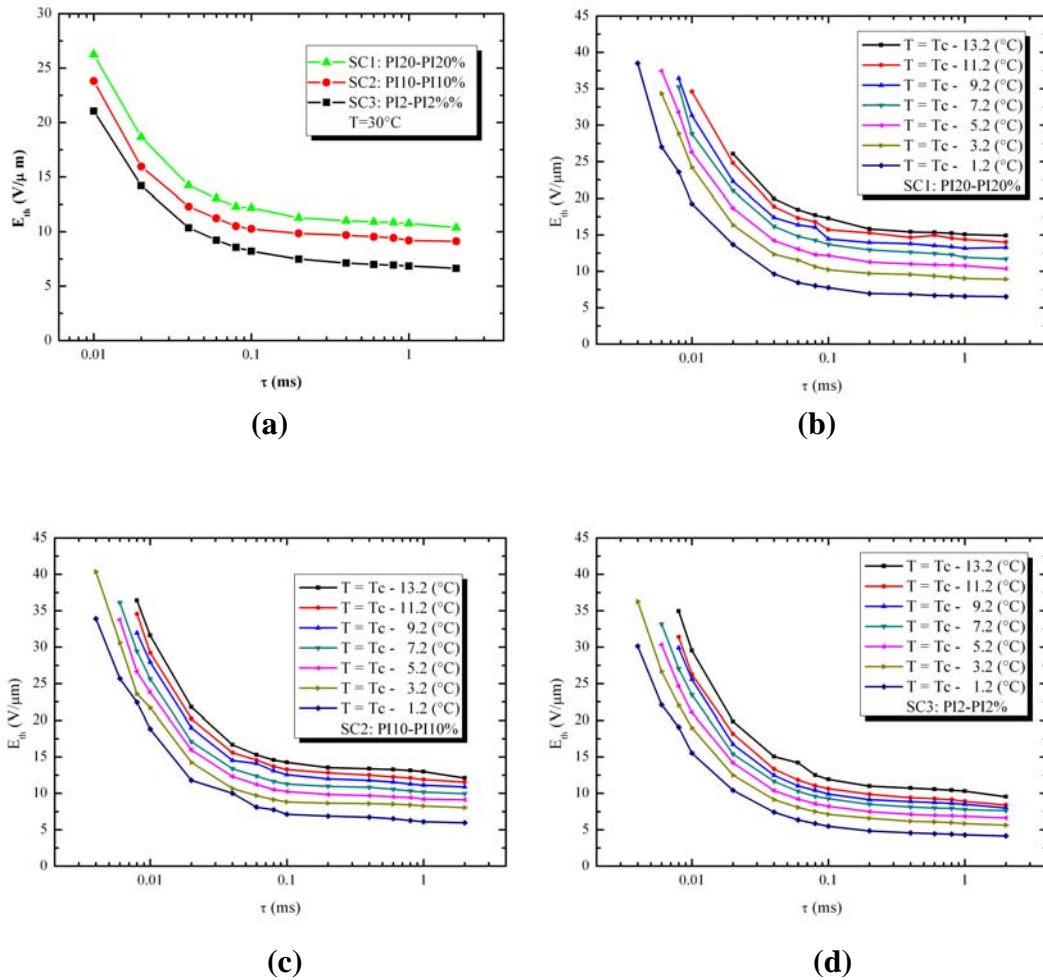


**Figure 5.4.** Threshold vs pulse durations: (a) at  $30^\circ\text{C}$  for the three different cells SC1, SC2 and SC3, (b, c and d) at different temperatures for the the three different cells SC1, SC2 and SC3 respectively.

The main macroscopic surface parameters for nematic anchoring are the surface tilt angle (pre-tilt) and the anchoring energy. The pre-tilt are measured as described in chapter 4 section 2 for the three surface treatments, obtaining  $2.0^\circ$ ,  $6.0^\circ$  and  $8.0^\circ$  respectively for 2% (SC3), 10% (SC2) and 20% (SC1) of PI

concentration. The anchoring strengths are  $1.0 \times 10^{-4} \text{ J/m}^2$ ,  $2.0 \times 10^{-4} \text{ J/m}^2$  and  $2.5 \times 10^{-4} \text{ J/m}^2$ , respectively for SC3, SC2 and SC1.

As the electric coherence length close to the order reconstruction threshold is much shorter than the anchoring extrapolation lengths corresponding to the observed anchoring energies, the nematic texture just below the transition values is homeotropic everywhere in all samples except in the biaxial wall in the middle of the cell and on two thin layers close to the boundary substrates, whose thickness is in all cases comparable with the electric coherence length itself. This means that the previous boundary parameters cannot influence the order reconstruction transition threshold as these relatively strong electric fields in practice decouple the biaxial wall dynamics by the anchoring conditions.

Another physical parameter that could be responsible of an apparent increase of the order reconstruction transition threshold is the thickness of the PI aligning layer, due to its dielectric properties. To evaluate the actual electric field acting on the nematic layer, due to the presence of the boundary PI thin films, one can consider that a typical cell of total thickness  $d$  is in fact composed by three layers: two boundary polymeric layers of thickness  $d_{PI}$  each one and the main LC layer of  $d - 2d_{PI}$  thickness, with dielectric constants  $\epsilon_{PI}$  and  $\epsilon_{LC}$  respectively. By applying the continuity of the normal component of the dielectric vector through the cell and calling  $E$  the applied electric field, we obtain the electric field  $E_{LC}$  acting in the liquid crystal layer:  $E_{LC}/E = d / ((d - 2d_{PI}) + 2d_{PI}\epsilon_{LC}/\epsilon_{PI})$

The aligning layers thicknesses have been measured both by an ellipsometric method and by X-ray reflectometry, with comparable results:  $(50 \pm 3) \text{ nm}$ ,  $(20 \pm 3) \text{ nm}$  and  $(6 \pm 2) \text{ nm}$  respectively for SC1, SC2 and SC3. Using the previous equation, the maximum electric drops in our samples in percentage at room temperature are 20%, 10% and 4% respectively for SC1, SC2 and SC3, and by considering the experimental data reported on figure 5.4.a, it is evident that the effect of the polymer aligning layers cannot explain the observed threshold variation for the three different surface treatments, which increases more than

50% by comparing data for the thinner PI film (SC3) with data for the thicker PI film (SC1).

As the previous surface parameters cannot explain the experimental observations, we performed numerical calculation to investigate this effect.

### **5.2.3. Bulk order reconstruction in symmetric cells**

The analysis of the biaxial transition is usually made by implicitly considering the case of an uniform wall, perfectly parallel to the planar boundary plates. This is a limit case which implies that the boundary physical parameters are perfectly uniform everywhere. This approach allowed to use a simplified one-dimensional description for the first dynamical numerical model [37]. If we admit that the biaxial wall could, for instance, undulate, the switching mechanism could be affected by this phenomenon. Recently a two-dimensional dynamical model suggests that small undulation of the biaxial wall could allow transitions through defect nucleation and disclination line movement [54]. The theoretical frame of this model has not been completely explained by the authors and the wall undulation is produced by using as initial condition a sinusoidal numerical perturbation in the middle of the cell. As an undulation of the biaxial wall could be generated by surface inhomogeneities and in a real cell it is very difficult to obtain a complete homogenous surface treatment, surface parameters must be taken into account. Surface inhomogeneities can be, for instance, related to local variations of the pre-tilt angle and/or to local variations of the anchoring energy and/or with local variation of the aligning film thickness [55] and/or local variations of the surface order [56]. To theoretically investigate the hypothesis of inhomogeneous surface treatments we solved numerically the governing equations (4.6 and 4.13 in chapter 3) in the bi-dimensional case. We used a finite element method (FEM) with adaptive mesh solver. The mesh is finer close to the boundary

surfaces and in the region where the biaxial wall appears with maximum mesh size of  $10nm$ . The modeled two-dimensional cell was  $1\mu m$  thick and  $2\mu m$  wide.

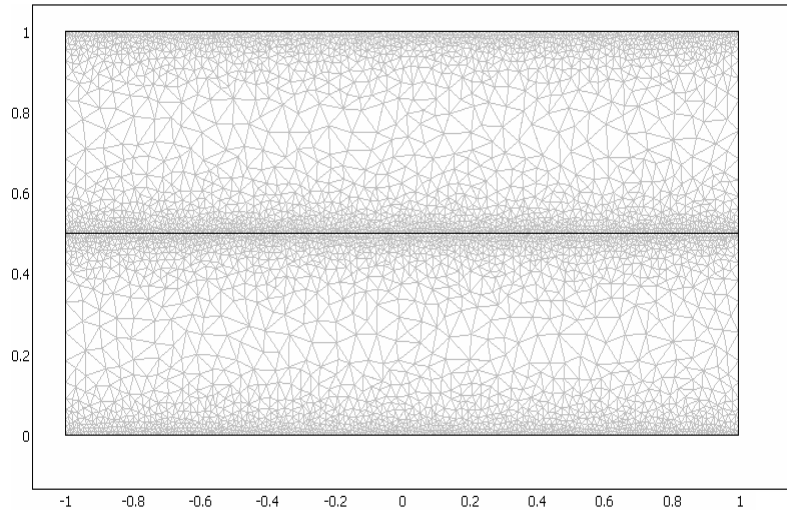


**Figure 5.5.** Bi-dimensional modeled cell discretized in triangular elements. Length are expressed in microns.

We start by investigating the cell SCN1 with a full symmetric situation and perfectly homogeneous boundary conditions on the horizontal plates, with a pre-tilt of  $\pm 1^\circ$ , which produces a perfect splayed texture. Then we investigate a second cell SCN2, whose boundary conditions on the planar plates simulate a small surface inhomogeneity. The electric field is applied at the time  $t = 0$  and it is always present during the calculations. For each point across the cell we compute the three eigenvalues of the  $Q$ -order tensor versus the time  $t$ , from which we calculate the director orientation and electric current density flowing through our cell.

In the case of SCN2, the anchoring conditions are periodic and the pre-tilt slowly varies with a sinusoidal modulation of  $1^\circ + 0.5^\circ \sin(2\pi x/\lambda)$  for the lower surface and  $1^\circ + 0.5^\circ \sin(2\pi x/\lambda + \varphi)$  for the upper substrate. By varying  $\lambda$  or  $\varphi$  we numerically control the cell inhomogeneity. In the following example of case SCN2, we fix  $\lambda = 2\mu m$  and  $\varphi = \pi/4$ , values which give the highest perturbation in the middle of the cell. In both cases SCN1 and SCN2, we assume an infinite anchoring energy. All calculations are performed by using periodic conditions on the vertical boundaries. In the case SCN1, when the applied field is strong enough to exceed the transition threshold, the biaxial wall vanishes uniformly as shown on figures 5.6, and, by looking at the calculated electric current flowing through the nematic material, we observe the formation of two well defined peaks, the fastest and largest one due to the dielectric realignment toward the homeotropic orientation of the two layers around the biaxial wall and the second one due to the biaxial wall breaking (full circle in Fig.5.7). In the case SCN2, the second electric peak, related to the nematic order reconstruction, practically does not exist any more, substituted by an irregular structure, wider in time and shorter in amplitude (empty circle in Fig.5.8), due to the fact that now the biaxial wall undulates and does not disappear everywhere at the same time (Figs.5.8). In this case, one observes a defect-mediated wall breaking. The practical suggestions of reference [52], to not put spacers in the active pixel area and to reduce the pixel area, are hence not sufficient to avoid this effect. In principle, even a weak distortion at the surface can give rise to a non homogeneous breaking of the wall and, as the electric current observation is high sensitive to this phenomenon, it can be used to detect and to distinguish uniform or inhomogeneous bulk nematic order reconstructions. Both cases have been widely observed in our experiments. Figure 5.8 shows that, in the uniform case, the biaxial wall has disappeared after  $85\mu s$  since the electric pulse application, while in the inhomogeneous case of figures 5.7.b and 5.7.c, the defects evolution is not completed after  $100\mu s$ . The width of the nematic order reconstruction electric peak in the uniform case is quite short ( $\sim 5\mu s$ ), while the electric response in the inhomogeneous case extends on a larger

time interval ( $\sim 30\mu\text{s}$ ). In the uniform case the energy of the biaxial wall is released everywhere in the sample in a short time, building a well defined electric peak, while in the inhomogeneous case, the energy is released firstly by forming couples of defects and then annealing them on a longer time scale, with a resulting electric signal without a well defined shape. Therefore the uniform wall disappearing is faster than the defect mediated wall breaking, in contrast with conclusions of reference [54]. We also underline that a small surface perturbation produces a wide undulation of the biaxial wall, whereas the artificial undulations reported in reference [54] have a much smaller scale, probably due to quenching by the uniform boundary conditions. Our investigations with very small surface pre-tilt show that the uniform and inhomogeneous transition mechanisms present practically the same threshold. There are threshold variations for high pre-tilt but are not sufficient to explain the experimental data. Only the boundary conditions determine which transition will take place and the actual path of the nematic order reconstruction can be easily checked by electric current observations.

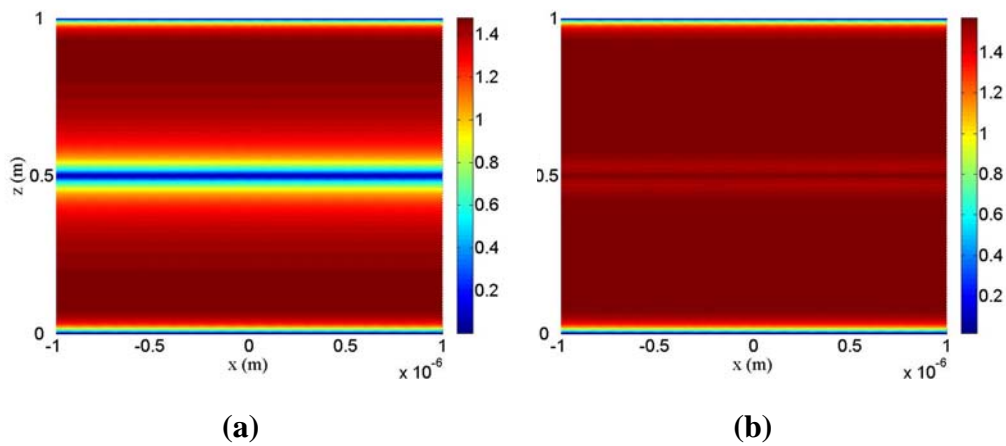


**Figure 5.6.** Time evolution of the biaxial wall in the case of homogeneous alignment. 50  $\mu\text{sec}$  (a), 85  $\mu\text{sec}$  (b) after the starting of the electric pulse.

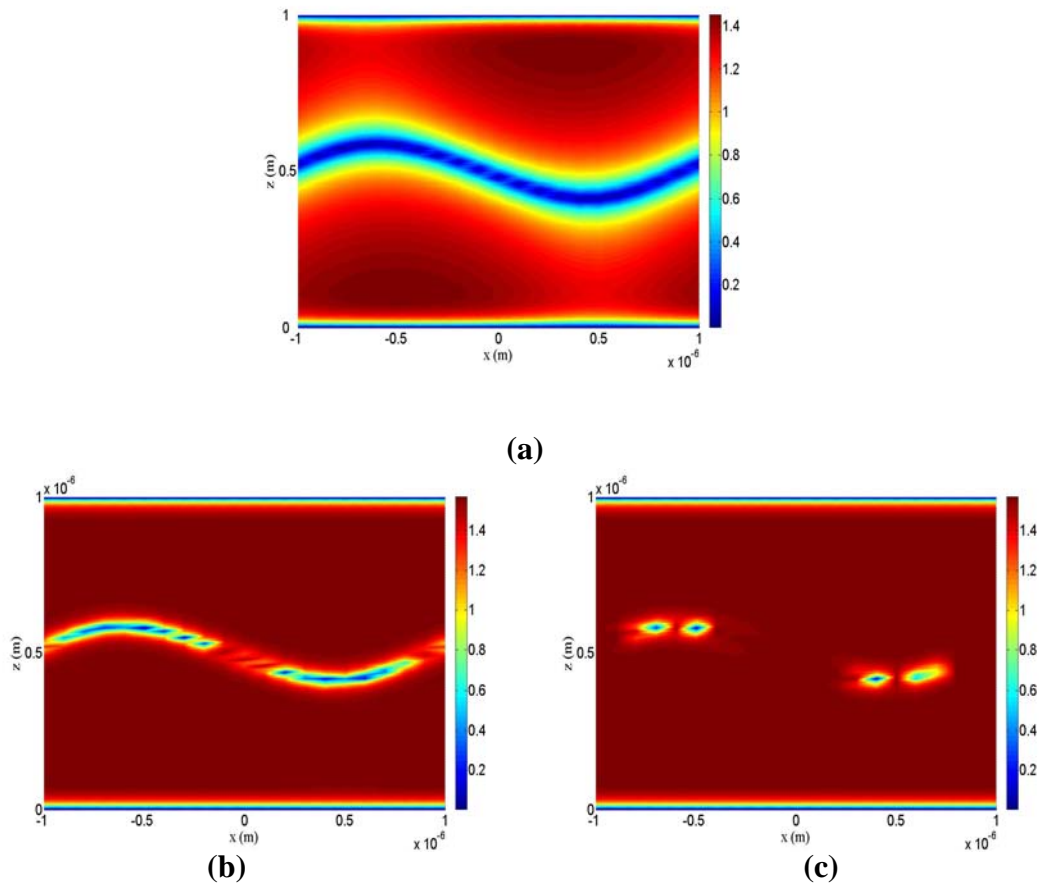


**Figure 5.7.** Time evolution of the biaxial wall in the case of inhomogeneous alignment. 50  $\mu\text{sec}$  (a), 85  $\mu\text{sec}$  (b), 100  $\mu\text{sec}$  (c) after the starting of the electric pulse.

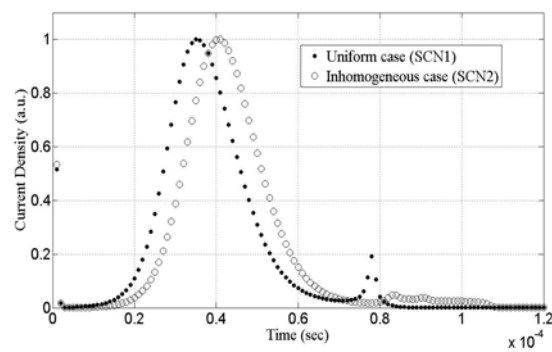


**Figure 5.8.** Numerical evolution of the electric current flowing through the cell vs time in the uniform case (full circles) and in the case of inhomogeneous case (empty circles).

The numerical model has also been tested to simulate the temporal positions of the order reconstruction peak for electric field larger than  $E_{th}$ . Figures 5.9 demonstrate the experimental (a) [38] and the numerical results (b) for the time position of the order reconstruction peak in the electric current as a function of  $1/E$ . The numerical data are well fitted by the phenomenological law  $1/\tau = (1/\tau_{th})(E^2 - E_{th}^2)/E_{th}^2$  proposed in reference [38], obtaining a further confirmation of a good agreement between the theoretical model and the experimental observations.  $\tau_{th}$  is the transition characteristic time and consists of three cascade process: the wall thinning time, the decrease of the nematic order due to the electrically induced constraint and the rebuilding of the nematic order in the vertical direction [52-53].

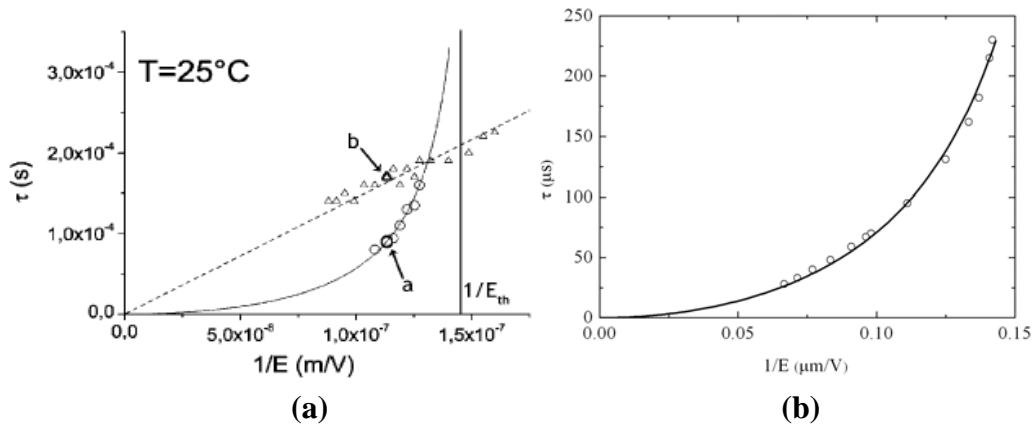


**Figure 5.9.** Reconstruction electric peak delay vs electric field above  $E_{th}$ . (a) experimental data represented in [38], (b) data obtained by the numerical model, fitted (continuous line) by the phenomenological law proposed in reference [38].



For a direct comparison between the theory and the experiments we plot in figure 5.10 the experimental thresholds measured for the cell SC1 compared with the numerical results of the cell SCN1. Figure 5.10 shows a good agreement between theory and experiment for electric pulse ranging from  $0.1\text{ms}$  to  $2\text{ms}$ , improving the previous results presented in reference [37]. The disagreement for pulses shorter than  $0.1\text{ms}$  could be solved by a better hydrodynamical description.

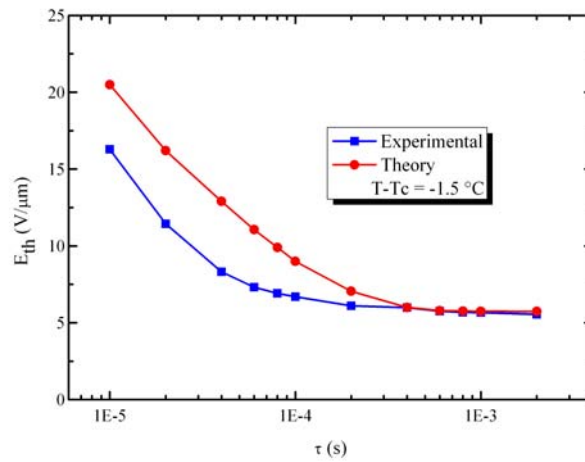


**Figure 5.10.** Comparison between theoretical data produced by the numerical model, and experimental data for the nematic order reconstruction threshold at  $T = T_c - 1.5^\circ\text{C}$ .

The previous theoretical analysis and the experimental observations cannot fully explain the experimental thresholds variation for cells with different surface treatments. As our model suggests that the biaxial wall could undulate and this undulation could be generated by same surface inhomogeneity and as in real cell it is very difficult to obtain a homogenous surface treatment, the anchoring surface inhomogeneity has also to be experimentally investigated. Any surface inhomogeneity can obviously be related with aligning films which do not cover regularly the boundary plate. This hypothesis can be checked by changing the PI

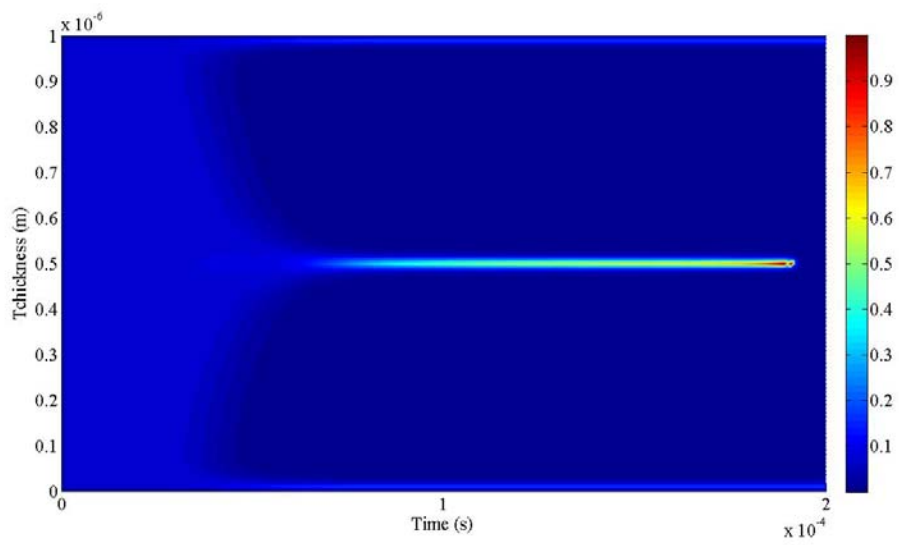
concentration for spin coating. In this way, the thickness of the aligning layer changes and affects the surface homogeneity. As we have seen, the order reconstruction transition thresholds are higher in the case of thicker aligning layers which corresponds in our case to the cell SC1 where high surface uniformity is expected. The transition threshold decrease for the cell SC2 and even more for the cell SC3. By checking the aligning films for those three cells by AFM technique we observe that the thicker film is the more homogeneous and the thinner film is irregular and it dose not cover uniformly the boundary plate. This behaviour seems to confirm our hypothesis.

## **5.3. Nematic order reconstruction in asymmetric cell**

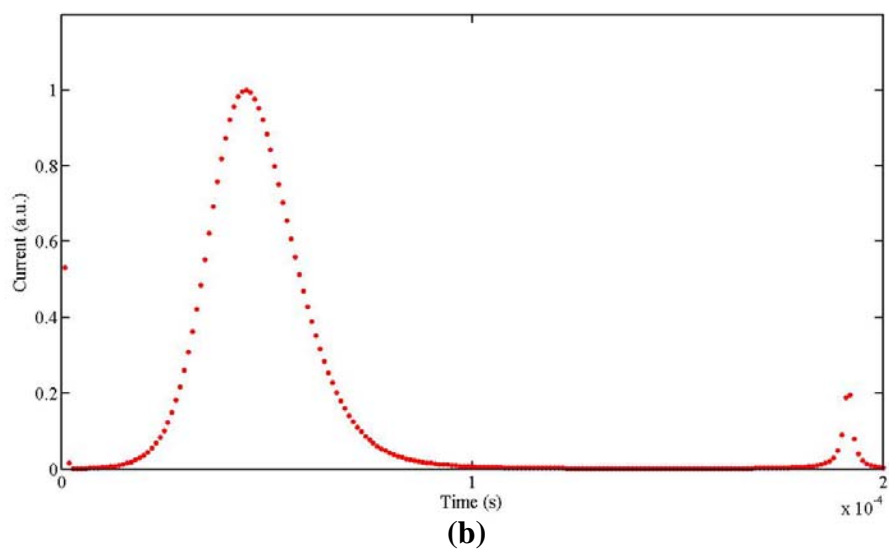
### **5.3.1. Numerical investigations of asymmetric cell**

To theoretically investigate the hypothesis of asymmetric cell, we fix the pre-tilt angle on the bottom surface and we change the opposite angle starting from the full symmetric case. If the pre-tilt angle  $\theta_l$  of the lower plate, for instance, is chosen much smaller than the one  $\theta_u$  of the upper plate, the first effect of this geometry is to build the biaxial wall close to the lower surface. To observe this effect, we have made a computer simulation of the one-dimensional cell ACN1 by fixing  $\theta_l = 1^\circ$  and  $\theta_u = 17^\circ$ , and for comparison we simulate also the one-dimensional symmetric cell C1 with  $\theta_l = \theta_u = 1^\circ$ . Now we observe the temporal evolution of  $Q$ -profile along the vertical direction. As described in paragraph 5.1.2, starting from the temporal evolution of the eigenvalues of the order  $Q$ -tensor, we compute the biaxiality  $\beta$  using equation 4.23 in chapter 3, and the

electric current flowing through our cell. All modeled cells were  $1\mu\text{m}$  thick, and we use fixed boundary conditions with a uniaxial  $Q$  which corresponds to the infinitely strong uniaxial anchoring. We can see in figure 5.11.a the calculated biaxiality  $\beta$  for the symmetric cell C1 where the maximum (red colour) is reached in the middle of the cell after about  $180\mu\text{s}$ , which corresponds to the electric order reconstruction peak time (figure 5.11.b). Figures 5.12 show the biaxiality  $\beta$  inside the asymmetric cell ACN1 at different applied electric fields (a) 10V, (b) 15V. Some weak biaxiality appears close to the boundaries but it is irrelevant for the biaxial transition and by looking at the calculated electric current, we observe a main peak coming from the molecular reorientation in between the boundary layers, followed by other electric structures (figure 5.13). Increasing the electric field, we can increase the biaxiality up to its maximum value  $\beta \sim 1$  (figure 5.14.a) and the transition  $I$  to  $B$  (figure 2.12 chapter 2) takes place. In this case, the electric current presents a well defined order reconstruction peak as shown in figure 5.14.b.

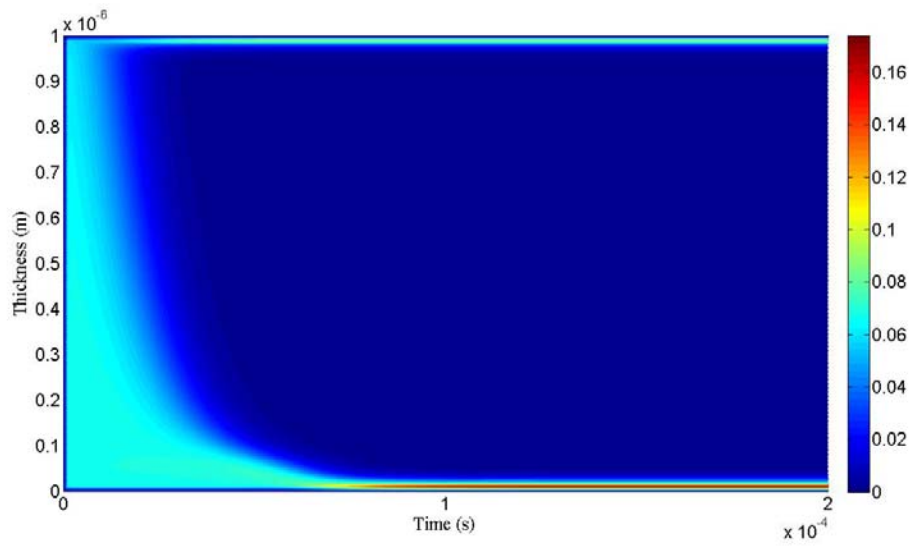


(a)

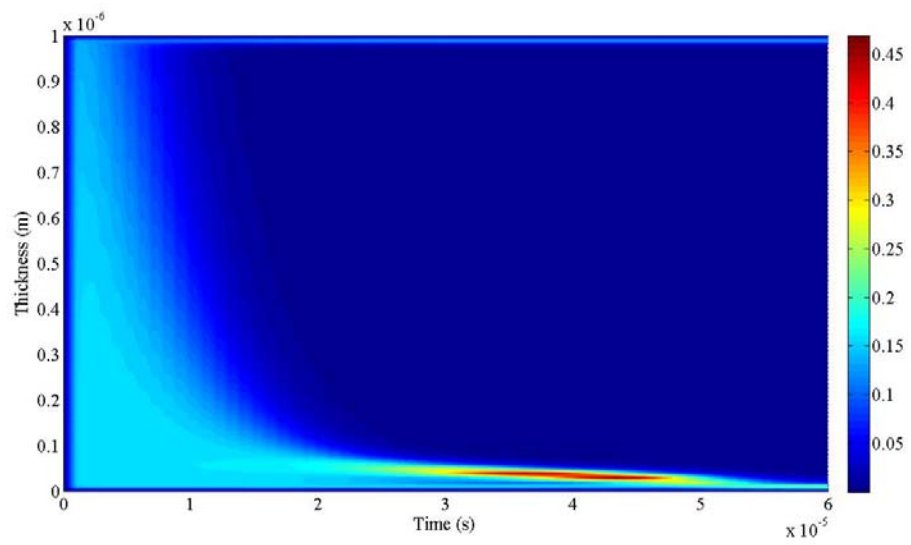


(b)

**Figure 5.11.** (a) Space-time evolution of the biaxiality and (b) the electric current, in the case of the symmetric cell C1 at 10V.



(a)



(b)

**Figure 5.12.** Space-time evolution of the biaxiality at (a) 10V and (b) 15V in the case of the asymmetric cell ACN1.

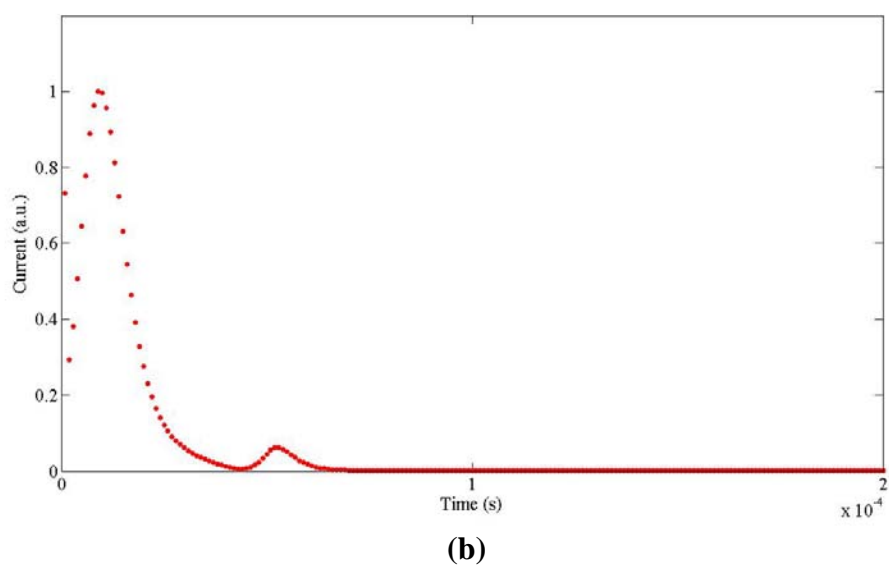
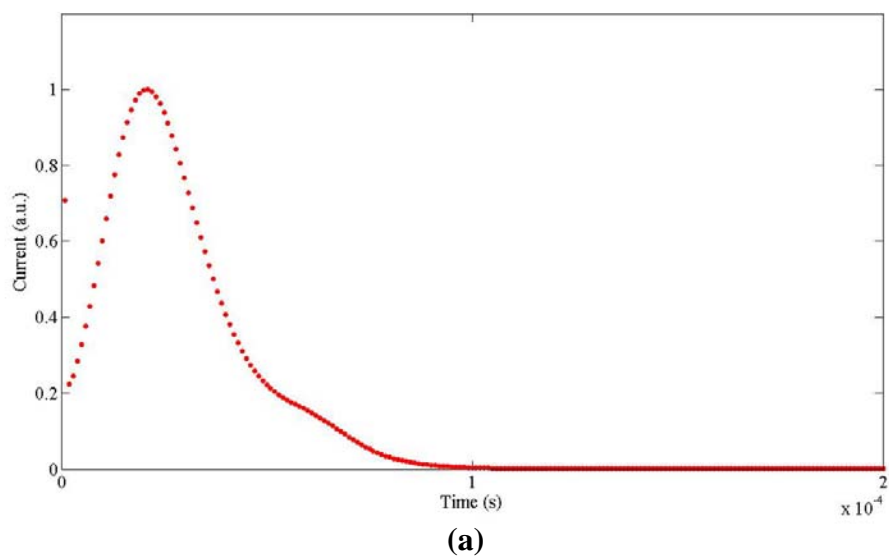
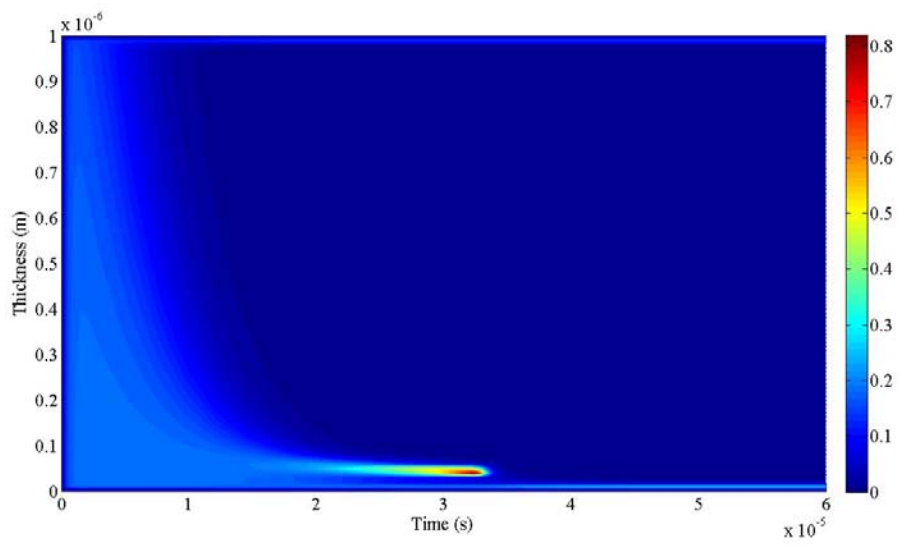
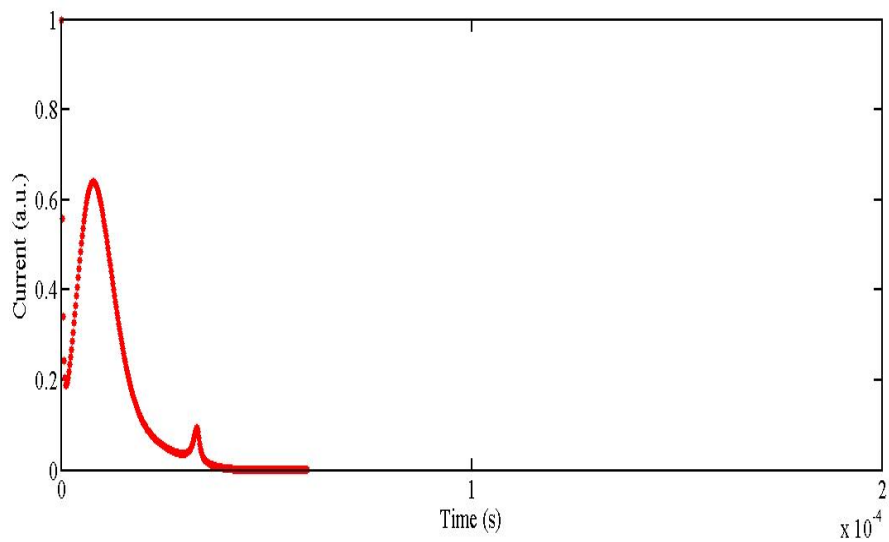


**Figure 5.13.** The electric current at (a) 10V and (b) 15V in the case of the asymmetric cell ACN1.



(a)



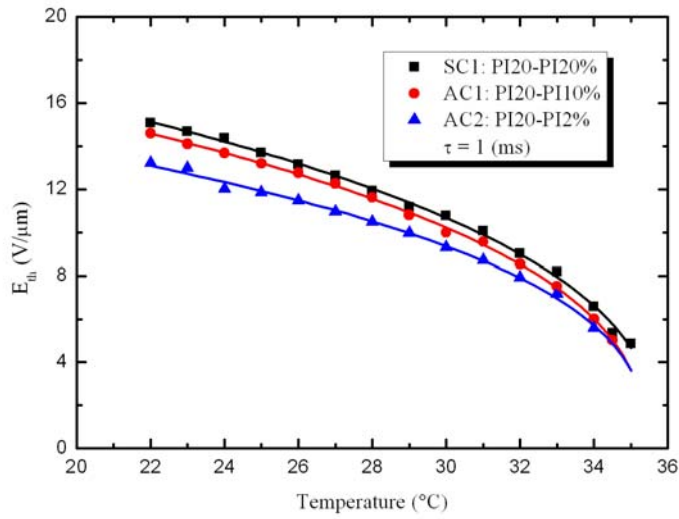
(b)

**Figure 5.14.** (a) Space-time evolution of the biaxiality and (b) the electric current, in the case of the symmetric cell ACN1 at 16V.

### 5.3.2. Experiments with asymmetric cells

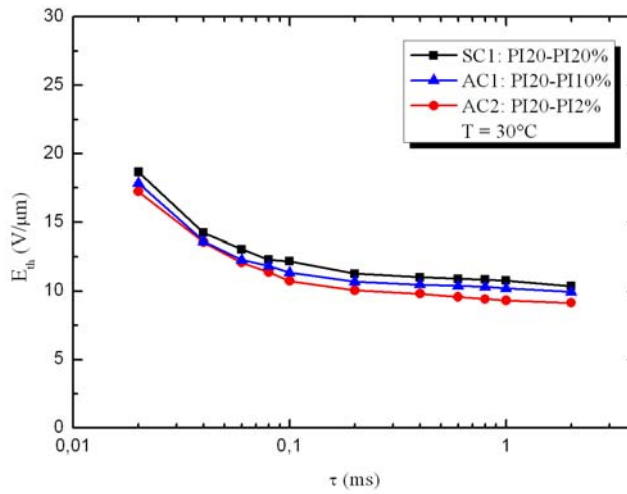
As it is crucial to distinguish surface effects by bulk phenomena for the electric field induced fast bistable textural switching between topologically distinct nematic configurations, we have made additional experiments to understand the connection between the pure bulk biaxial order reconstruction and surface induced transitions. We have used asymmetric cells which allow the formation of the biaxial wall close to a surface, on suitable surface tilt angles. Starting from our standard cell SC1 described above, where high symmetry and uniformity are expected, we made asymmetric cells AC1 and AC2 by keeping one surface identical to the surfaces used for the SC1 cell, with a pre-tilt of  $8^\circ$ , while the other one is changed by varying the polyimide concentration in the starting mixture 10% for (AC1) cell, pre-tilt of  $6^\circ$ , and 2% for (AC2) sample, pre-tilt of  $2^\circ$ . As described above and in chapter 4, all cells have thickness of about  $2\mu\text{m}$ . For a direct comparison with all previous cited experiments, cells were filled with the 5CB liquid crystal and investigated using the same experimental setup already reported in chapter 4. First of all we investigated the dependence of the transition threshold on the temperature for the three following cells: SC1, AC1 and AC2. This allows a direct comparison between symmetric and asymmetric samples. We present in figure 5.15 the dependence of the observed threshold field versus the cell temperature at fixed  $\tau = 1\text{ms}$  for the three cells SC1, AC1 and AC2. The general behaviour of the two kinds of cells (symmetric and asymmetric) seems similar. However, for a complete comparison we study the dependence of the threshold field on the pulse duration  $\tau$ .





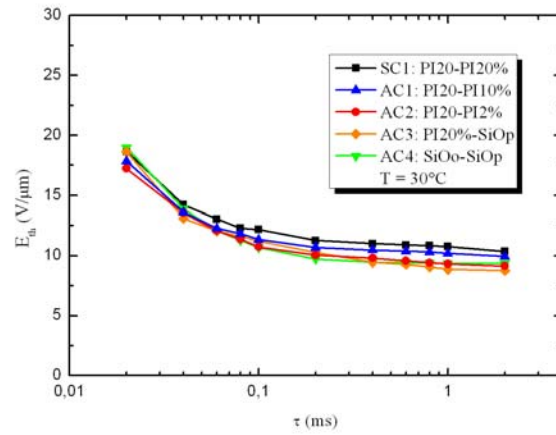
**Figure 5.15.** Temperature dependence of the threshold for three different cells SC1, AC1 and AC2 at  $\tau = 1\text{ ms}$ . The fitting curves represent the power law  $E_{th} \propto (T_c - T)^\alpha$  give  $\alpha = 0.390$  for SC1,  $\alpha = 0.388$  for AC1 and  $\alpha = 0.374$  for AC2.

Figure 5.16 presents experimental results of  $E_{th}$  versus  $\tau$  for the three samples SC1, AC1 and AC2. The behaviour of the two asymmetric cells AC1 and AC2 is again similar with the case of the symmetric cell SC1. The highest threshold is observed for the symmetric cell SC1 and by decreasing slightly the cell symmetry, the threshold decreases and has lower values for the less symmetric cell AC2. In principle, for the uniform symmetric cell SC1, the applied electric field tends to concentrate the biaxial wall parallel to the containing plates, in the middle of the cell, as represented by the simulation of cell C1 in figure 5.11; while for asymmetric cells, the difference of the surface treatments shifts the wall toward the surface with low pre-tilt, in a way that should be similar at the simulation reported for the cell ACN1 in figure 5.14.

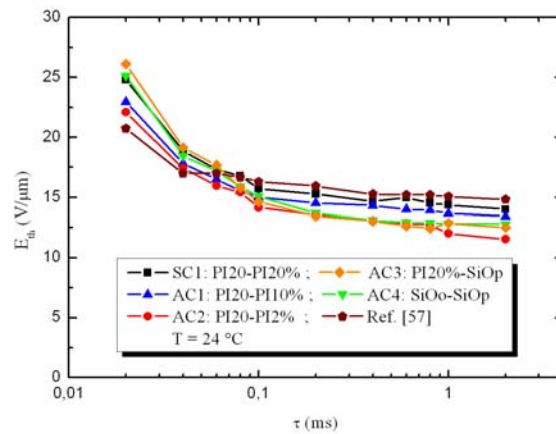


**Figure 5.16.** Threshold vs pulse durations at 30°C for the three different cells SC1, AC1 and AC2.

A first comparison between pure bulk effects and surface induced transitions can be found in ref.[57] and ref. [58]. For a better understanding of these phenomena, we prepared the cell AC3 by using grazing angle  $\text{SiO}_x$  evaporations, obtaining a planar-oblique texture, which is well known as a standard cell for the first order anchoring breaking transition [58] and a last cell AC4 with  $\text{SiO}$  planar alignment on one substrate and uniform oblique anchoring by spin coating a PI20% film on the other plate. The symmetrical cell SC1 should be driven by the bulk effect of nematic order reconstruction [36-38], while the more asymmetric cells AC3 and AC4 will present surface induced effects [57, 58]. Figures 5.17 show the threshold dependence on the pulse width at two different temperatures for the symmetric cell SC1 and the series of asymmetric cells described above.



(a)



(b)

**Figure 5.17.** Threshold vs pulse durations at 30°C (a) 24°C (b) for the cells SC1, AC1, AC2, AC3 and AC4.

As expected, all cells exhibit a similar behaviour. The threshold field decreases from its highest values for the SC1 cell and it reaches a minimum for the three more asymmetric cells AC2, AC3 and AC4, whose electro-optical behaviour is practically superposed. This is due to the effect of the boundary, which plays an important role in the creation of the biaxial wall. As the cell AC2 has a pre-tilt angle  $\theta_l \sim 1-2^\circ$ , we are sure to obtain a volume biaxial order reconstruction and not

a surface anchoring breaking [57]. However, the behaviour of our cells is globally equivalent to the cases of [57-58] where the switching between topologically inequivalent textures is obtained by anchoring breaking. The main difference between the transition reported in ref. [57-58] and our new experiments is that to break more easily the anchoring one needs to use special surfaces, which possess weak anchoring strength, which is difficult to obtain in practice. In our case, we need nematics with high dielectric anisotropy  $\Delta\epsilon$ , which are also required in the case of anchoring breaking, but we do not need the weak anchoring condition. We can maintain the usual strong anchoring treatments which are easier to realize in practice. The biaxial order reconstruction will overcome the difficulty to achieve the mechanism of real surface anchoring breaking. With very strong planar anchoring, the biaxial order reconstruction is the unique mechanism which is able, for instance, to realign the nematic director parallel to the electric field. In all the investigated asymmetric cells, the biaxial wall disappears close to a planar or quasi-planar substrate, independently by the anchoring strength. We have also experimentally demonstrated surface order reconstruction in asymmetric cells where the planar anchoring is obtained by PVA rubbed film, which are well known to give strong anchoring and which are not compatible with the model of anchoring breaking. Also in this case, the transition the transition threshold is comparable with the other asymmetric cells.

## **5.4. Experiments with doped nematics**

The optimization of the biaxial order reconstruction implies the use of uniaxial nematics which can present transient biaxial states. In this chapter we present experimental data on mixtures with an usual nematic with high  $\Delta\epsilon$  doped with

materials which raise or decrease the biaxial tendency of the mixture. We describe here new experiments of order reconstruction by doping the 5CB with various kinds of low concentration compounds which vary the biaxial properties of the mixture, showing variations of  $E_{th}$  with respect to the pure 5CB.

The pure nematic 5CB has a nematic-isotropic transition temperature at  $T_c \approx 35^\circ\text{C}$  and as soon as we add any dopant, we observe a change in  $T_c$ , which depends on the dopant itself and the dopant concentration. To evaluate the real effect of the doping, hence we present data by using the reduced temperature ( $T_c - T$ ).

#### **5.4.1. Doping with MBBA**

We first used as dopant the n-4'-**MethoxyBenzylidene-n-ButylAnilin** (MBBA) which is nematic between  $16^\circ\text{C}$  and  $46^\circ\text{C}$  and has negative dielectric anisotropy  $\Delta\epsilon_{\text{MBBA}} = -0.7$  at  $25^\circ\text{C}$  with concentration 2% weight in 5CB. The mixture 5CB with 2% MBBA has a mean dielectric constant  $\Delta\epsilon_{\text{Mixture}} = 11.6$  about 10% smaller than pure 5CB and hence the transition threshold for the order reconstruction should increase. But the negative dielectric anisotropy is expected to increase the biaxiality in the planar wall. We have measured for this mixture  $E_{th}$  versus the temperature at fixed  $\tau = 1\text{ms}$ , the data are plotted in figure 5.18. Comparing with pure 5CB, the cell filled with doped 5CB shows practically the same temperature behaviour but the threshold values decreased of about 10%.

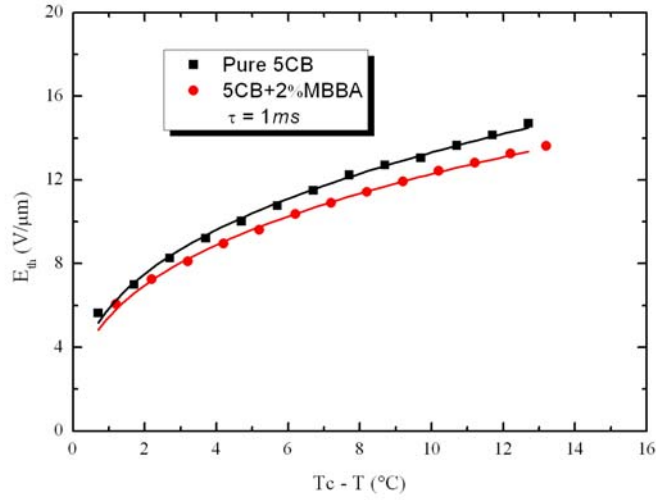


**Figure 5.18.** Temperature dependence of the threshold for 5CB doped with 2% MBBA compared to the pure 5CB. The fitting curves represent the power law  $E_{th} \propto (T_c - T)^\alpha$  give  $\alpha = 0.390$  for pure 5CB,  $\alpha = 0.401$  for 5CB+2% MBBA.

#### 5.4.2. Doping with RM257

We now present results on the influence of the oligomers on the nematic order reconstruction behaviour. The mixture was 2% weight of diacrylate monomer (RM257 from Merck) in 5CB liquid crystal. A low percentage (2% of monomer weight) of photoinitiator Darocur 1173 was also used. The monomer RM257 has negative dielectric anisotropy  $\epsilon_a \approx -2$  and a stable nematic phase in the range of temperature 70-126°C. In our study we investigate the effect of the monomer on the order reconstruction threshold before and after UV curing. Experimental results are reported in figure 5.19. We can notice that after UV curing the cell for 30s, the threshold decreases of about 7% with respect to the same cell before UV curing and about 10% with respect to cell filled with pure 5CB. By fitting the

experimental data to the power law  $(T_c - T)^\alpha$  we obtain  $\alpha = 0.40$  before UV curing and  $\alpha = 0.39$  after UV curing. The fit is shown in figure 5.18 by the solid line.

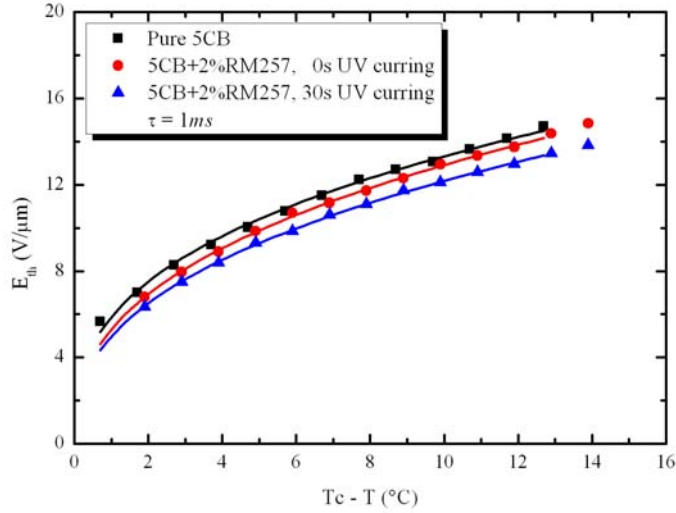


**Figure 5.19.** Temperature dependence of the threshold for pure 5CB, 5CB doped with 2% RM257 without UV curing (square) and 5CB with 2%RM257 after 30s UV curing (circle). The fitting curves represent the power law  $E_{th} \propto (T_c - T)^\alpha$ ,  $\alpha = 0.40$  for 0 s UV curing,  $\alpha = 0.39$  for 30s UV curing.

### 5.4.3. Doping with ferroelectric particles BaTiO<sub>3</sub>

Now we present experimental results obtained using a ferroelectric nano-powder as dopant. The nanoparticles are so small (less than 50 nm) that they must not disturb too much the liquid crystal orientation. Here we report studies of the order reconstruction threshold of a nematic liquid crystal mixture containing ferroelectric BaTiO<sub>3</sub> particles. This material has tetragonal crystal structure with [001] polar axis and a spontaneous polarisation of 26  $\mu\text{C}/\text{cm}^2$  at room temperature. The dielectric constant of the BaTiO<sub>3</sub> single crystal is about 170 in the direction parallel to the polar axis and 2.9 perpendicular to the polar axis and

its Curie temperature  $T_{\text{Curie}} \approx 110^\circ\text{C}$ . We used a mixture of 5CB and 0.5% wt  $\text{BaTiO}_3$  ferroelectric nanoparticles. The concentration of the particles in our nematic must be less than 1%wt, otherwise they will start to sediment. In the same temperature scale we plot in figure 5.20 the temperature dependence of  $E_{th}$ , for pure 5CB and for the 5CB liquid crystal doped with  $\text{BaTiO}_3$ . One can see that the general behaviour of both cells is quite similar, but now the presence of ferroelectric particles in the liquid crystal increases of about 3.5% the order reconstruction threshold. The small increases of the threshold values can be explained by a decrease of the biaxiality inside the cell. These ferroelectric nanoparticles are in fact expected to increase the nematic order.

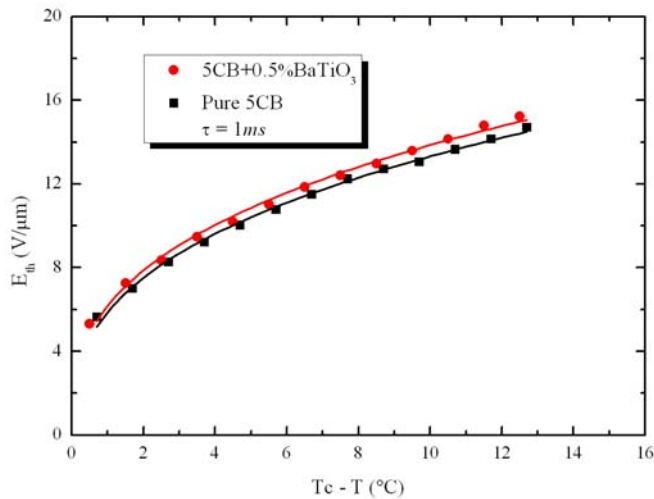


**Figure 5.20.** Dependence of the order reconstruction threshold on the temperature for pure 5CB and for a cell filled with the mixture of 5CB and 0.5% wt of  $\text{BaTiO}_3$  ferroelectric nanoparticles. The fitting curves represent the power law  $E_{th} \propto (T_c - T)^\alpha$ ,  $\alpha = 0.39$  for pure 5CB,  $\alpha = 0.40$  for 5CB+0.5%  $\text{BaTiO}_3$ .





# **CHAPTER VI**

**~Conclusions~**



# Chapter VI

## Conclusions

The work of this thesis has been focused on the study of the nematic order reconstruction induced by electric field, with an interesting mix of experimental and theoretical parts. In a symmetric splayed cell subjected to a strong electric field, the nematic order in the directions orthogonal to the long axis of the order tensor is dielectrically unfavourable and it is rebuilt along the applied electric field, when this one exceeds a certain threshold. This allows to connect non topologically equivalent textures, i.e. to produce bistability. The main experimental activities were investigations of the nematic biaxial order transition in thin splayed cells. For this purpose we have studied several cells by changing the surface properties in both symmetric and asymmetric cases. We have experimentally demonstrated the existence of relevant surface effects on the bulk nematic order reconstruction. These results have been confirmed by numerical simulations, using a  $Q$ -tensor representation for the free energy. The structure of the biaxial wall that precedes the order reconstruction, is in fact directly related to the anchoring uniformity, which plays a very important role to determine various mechanisms of transition, from the uniform disappearing of the wall to the formation of couples of defects or with absorption on the surfaces. We have also demonstrated that the so-called “anchoring breaking” can be seen as a particular case of reconstruction of the order in proximity of a surface. Moreover, we have also experimentally demonstrated the possibility to increase or decrease the tendency toward the biaxial order by using an usual uniaxial nematic doped by suitable materials.



## ~~Bibliography~~



# Bibliography

- [1] P.G. De Gennes, J. Prost: The Physics of Liquid Crystals, 2nd ed. (Clarendon Press, Oxford) (1993)
- [2] P. Yeh, C. Gu: Optics of Liquid Crystal Displays, (John Wiley& Sons, New York) (1999)
- [3] G. Barbero, I. Dozov, J.F. Palierne, G. Durand, Phys. Rev. Lett. **56**, 2056 (1986)
- [4] H. Brandt, Mol. Cryst. Liq. Cryst. Lett. **3**, 147 (1986)
- [5] I. Dozov, G. Barbero, J.F. Palierne, G. Durand, Europhys.Lett. **1**, 563 (1986)
- [6] F.C. Frank, Disc. Faraday Soc. **25**, 19 (1958)
- [7] J. Nehring, A.Saupe, J. Chem. Phys. **54**, 337 (1971)
- [8] E. Dubois-Violette, O. Parodi, J. Phys (Paris) Colloq. **30**, C4-57 (1969)
- [9] H. Yokoyama, Phys. Rev. E **55**, 2938 (1997)
- [10] G. Barbero, S. Ponti, Phys. Lett. A **239**, 267 (1998)
- [11] S. Dickman, J. Eschler, O. Cossalter, and D. A. Mlynski, SID'93 Dig 638, (1993)
- [12] K.Schiele and S. Trimper, Phys. Status Solidi B **118**, 267 (1983)
- [13] D. W. Berreman and S. Meiboom, Phys. Rev. A **30**, 1955, (1984)
- [14] A. L. Alexe-Ionescu, Phys. Lett. A, **180**, 456 (1993)
- [15] A. Rapini and M. Papoular J. Physique Coll. **30** C4 54, (1969)
- [16] L. M. Blinov and V. G. Chigrinov: Electrooptic Effects in Liquid Crystal Materials, (Springer-Verlag, New York) (1994)
- [17] F. C. Frank, Discuss. Faraday Soc. **25**, 19, (1978)
- [18] N. D. Mermin, Rev. Mod. Phys. **51**, 591, (1979)
- [19] N. Schopohl, T.J. Sluckin, Phys. Rev. Lett. **59**, 2582 (1987)
- [20] M. Schadt and W. Helfrich, Appl. Phys. Lett. **18**, 127 (1971)
- [21] J. Ferguson, U.S. Patent No. 3,731,986 (1973)
- [22] G.H. Heilmeyer and L.A. Zanoni, Appl. Phys. Lett. **13**, 91 (1968)
- [23] T. Uchida, H.Seki, C.Shishido, M. Wada, Proceedings of the SID **22**, 41 (1981)
- [24] D. L. White and G. N. Taylor, J. Appl. Phys. **45**, 4718 (1974)
- [25] M. Oh-e and K. Kondo, Appl. Phys. Lett. **67**, 3895 (1995)



- [26] M. Oh-e and K. Kondo, *Liq. Cryst.* **22**, 379 (1997)
- [27] W. Greubel, U. Wolf and H. Kruger, *Mol. Cryst. Liq. Cryst.* **24**, 103 (1973)
- [28] D. K. Yang, J. L. West, L.C. Chien and J.W. Doane, *J. Appl. Phys.* **76**, 1331 (1994)
- [29] D. W. Berreman and W. R. Heffner, *Appl. Phys. Lett.* **37**,109 (1980)
- [30] R. Barberi and G. Durand, *Appl. Phys. Lett.* **58**, 2907 (1991)
- [31] R. Barberi, M. Giocondo and G. Durand, *Appl.Phys. Lett.* **60**, 1085, (1992)
- [32] I. Dozov, Ph. Martinot-Lagarde, E. Polossat, I. Lelidis, M. Giocondo, G. Durand, *Proceedings of SPIE* **3015**, 61 (1997)
- [33] I. Dozov, M. Nobili, G. Durand, *Appl. Phys. Lett.* **70**, 1179(1997)
- [34] G. P. Bryan-Brown, C. V. Brown, J.C. Jones, E. L. Wood, I. C. Sage, P. Brett, J. Rudin, *SID Intl. Symp. Digest Tech.Papers* **28**, 37 (1997)
- [35] E. L. Wood, G. P. Bryan-Brown, P. Brett, A. Graham, J. C. Jones, and J. R. Hughes *SID Intl. Symp.Digest Tech. Papers* **31**, 124 (2000)
- [36] Ph. Martinot-Lagarde, H. Dreyfus-Lambeze, and I. Dozov, *Phys. Rev. E* **67**, 051710 (2003)
- [37] R. Barberi., F. Ciuchi, G. Durand, M. Iovane, D. Sikharulidze, A. Sonnet, and E. Virga, *Eur. Phys. J. E* **13**, 61(2004)
- [38] R. Barberi, F. Ciuchi, G. Lombardo, R. Bartolino, and G. Durand, *Phys. Rev. Lett.* **93**, 137801 (2004)
- [39] P. G. de Gennes, *Phy. Lett. A* **30**, 454 (1969)
- [40] J. E. Anderson, P. Watson, and P. J. Bos, *LC3D: Liquid Crystal Display 3-D Directory Simulator, Software and Technology Guide*. Reading, MA: (Artech House) (1999)
- [41] A. Sonnet and E. Virga, *Phys. Rev. E* **64**, 031705 (2001).
- [42] Y. W. Kwon and H. Bang: *The Finite Element Method Using MATLAB* (BocaRaon, FL: CRC Press) (2000)
- [43] G. Lombardo Ph.D. Thesis University of Reggio Calabria (2002)
- [44] J. E. Anderson, C. Titus, P.Watson, and P. J. Bos, *Soc. Inf. Display Tech. Dig.* **31**, 906 (2000)
- [45] B. Ratna, R. Shashidhar, *Mol. Cryst. Liq. Cryst.* **42**, 113 (1977)

- [46] D. Dunmur, A. Fukuda, and G. Luckhurst: Physical Properties of Liquid Crystals (INSPEC,London-UK) ( 2001)
- [47] A.M. Sonnet, and S. Hess, Defects in Liquid Crystals: Computer Simulations, Theory and Experiments, 17-36 (Klumer Academic Publishers) (2000)
- [48] P. Kaiser, W. Wiese, S. Hess, J. Non-Equilib. Thermodyn **17**, 153 (1992)
- [49] T.J. Scheffer, J. Nehring, J. Appl. Phys, **48**, 1783 (1977)
- [50] S. Palto, R. Barberi, M. Iovane, V. V. Lazarev and L. Blinov, Mol. Materials **11**, 277 (1999)
- [51] L. Komitov, G. Hauck, and H. D. Koswig, Phys. Status Solidi A **97**, 645 (1986)
- [52] S. Joly, I. Dozov, and P. Martinot-Lagarde, Phys. Rev. Lett. **96**, 019801 (2006)
- [53] R. Barberi, F. Ciuchi, H. Ayeb, G. Lombardo, R. Bartolino, and G. Durand, Phys. Rev. Lett. **96**, 019802 (2006)
- [54] Y. Zhang, B. Wang, D. B. Chung, J. Colegrove, and P. J. Bos, SID Proceeding **36**, 1782 (2005)
- [55] A. Alexe-Ionescu, R. Barberi, G. Barbero, J. Bonvent, and M. Giocondo, Appl. Phys. A **61**, 425 (1995)
- [56] R. Barberi and G. Durand, Phys. Rev A **41**, 2207 (1990)
- [57] I. Dozov, M. Nobili, G. Durand, Appl. Phys. Lett. **70**, 1179 (1997)
- [58] I. Dozov, P. Martinot-Lagarde., Phys. Rev. E **58**, 7442 (1998)

